HHS Public Access

Author manuscript

J Theor Biol. Author manuscript; available in PMC 2023 December 21.

Published in final edited form as:

J Theor Biol. 2022 December 21; 555: 111283. doi:10.1016/j.jtbi.2022.111283.

Modeling of ionizing radiation induced hair follicle regenerative dynamics

Cecilia Duran[a,b], **Manuel Barcenas**[a], **Qixuan Wang**[a,b,*]

[a]Department of Mathematics, University of California, Riverside, CA, USA

[b]Interdisciplinary Center for Quantitative Modeling in Biology, University of California, Riverside, CA, USA

Abstract

Hair follicles (HFs) are stem-cell-rich mammalian mini-organs that can undergo cyclic regenerations over the life span of the organism. The cycle of a HF consists of three consecutive phases: anagen—the active proliferation phase, catagen—the degeneration phase, and telogen—the resting phase. While HFs undergo irreversible degeneration during catagen, recent experimental research on mice shows that when anagen HFs are subject to ionizing radiation (IR), they undergo a transient degeneration, followed by a nearly full regeneration that makes the HFs return to homeostatic state. The mechanisms underlying these IR-induced HF regenerative dynamics and the catagen degenerative dynamics, remain unknown. In this work, we develop an ODE type cell differentiation population model to study the control mechanisms of HF regeneration. The model is built based on current theoretical knowledge in biology and mathematically formulated using feedback mechanisms. Model parameters are calibrated to IR experimental data, and we then provide modeling results with both deterministic ODE simulations and corresponding stochastic simulations. We perform stability and bifurcation analyses on the ODE model, which reveal that for anagen HFs, a low spontaneous apoptosis rate secures the stability of the HF homeostatic steady state, allowing the HF to regenerate even when subject to strong IR. On the other hand, the irreversible degeneration during catagen results from both strong spontaneous apoptosis rate and strong apoptosis feedback. Lastly, we perform sensitivity analysis to identify key parameters in the model to validate these hypotheses.

Keywords

Hair follicle; Cell differentiation model; Growth and regeneration; Radio-therapy; Dynamical system; Stability analysis; Bifurcation analysis

[*]Corresponding author at: Department of Mathematics, University of California, Riverside, CA, USA. qixuanw@ucr.edu (Q. Wang).

Declaration of competing interest

The authors declare that they have no known competing financial interests or personal relationships that could have appeared to influence the work reported in this paper.

CRediT authorship contribution statement

Cecilia Duran: Conceptualization, Methodology, Software, Validation, Formal analysis, Writing – original draft, Writing – review & editing. **Manuel Barcenas:** Software, Formal analysis. **Qixuan Wang:** Conceptualization, Methodology, Software, Validation, Formal analysis, Investigation, Resources, Data curation, Writing – original draft, Writing – review & editing, Supervision, Funding acquisition.

1. Introduction

Hair follicles (HFs) are mammalian skin mini-organs which are rich in stem cells. Unlike many other tissues and organs, HFs undergo cycles of regeneration throughout the lifetime of the organism. Each HF growth cycle consists of three phases: anagen, the active proliferation phase; catagen, the degeneration phase; and telogen, the quiescent phase. The dynamics of a HF growth cycle are briefly summarized below.

During telogen, a HF rests in its smallest possible size made up of three main compartments: the bulge, hair germ (HG), and the dermal papillae (DP). (Fig. 1A). The bulge is a niche of *bona fide* epithelial stem cells. Underneath the bulge lies the HG, which houses short-lived epithelial progenitors derived from bulge stem cells. The DP marks the bottom of the HF, it contains specialized fibroblasts and serves as the signaling "command center". The cells of a telogen HF are relatively biochemically and proliferatively quiescent (Stenn and Paus, 2001; Paus and Foitzik, 2004).

During late telogen, DP cells become activated and this marks the onset of anagen. Once activated, DP cells produce various signaling factors, which cooperatively activate proliferation of HF epithelial cells and initiate hair growth. At the beginning of anagen, HG cells give rise to fast-dividing epithelial hair matrix (Mx) cells (Fig. 1B). Mx cells are transient-amplifying (TA) cells that have limited mitotic potential (Hsu et al., 2014) yet show a fast cell cycle time of only 12–13 h in mice and 24 h in humans (Van Scott et al., 1963; Malkinson and Keane, 1978). Meanwhile, the bulge stem cells also become activated and contribute to the formation of the outer root sheath (ORS) which forms the outer epithelial layer of the HF. Mx cells surround the DP and also connect to the lower ORS (Fig. 1B)

As Mx continues to grow, its cells start to differentiate to several types of terminally differentiated (TD) cells, including the hair shaft (HS) and the inner root sheath (IRS). ORS cell proliferation is the main driving force of the downward HF growth, and it occurs in response to various signaling factors, including *Sonic Hedgehog* (Shh) and *Wingless/Integrated* (Wnt) signaling ligands (Van Mater et al., 2003; Celso et al., 2004; Zhang et al., 2016; Vidal et al., 2005; Wang et al., 2000; Sato et al., 1999; Huelsken et al., 2001). When a HF grows to a certain length, further downward growth stops, and the HF reaches a dynamic equilibrium that can be maintained for an extended period of time. Despite the relatively constant and stable HF length, its lower compartments (including DP, Mx and lower ORS) remain active, in the way that: (1) cells actively participate in signaling dynamics, and (2) epithelial cells actively divide in response to various signals. In contrast, in the upper HF, as DP and Mx move downward away from the bulge, the signaling source disappears, thus bulge stem cells and upper ORS cells return to quiescence.

Throughout anagen there are only very few apoptotic cells (Van Scott et al., 1963; Malkinson and Keane, 1978). However, upon transition to early catagen, a coordinated apoptotic wave originates in the Mx and propagates upward through the rest of epithelial HF compartments (Lindner et al., 1997; Müller-Röver et al., 1999; Straile et al., 1961; Haake and Polakowska, 1993; Paus et al., 1993; Polakowska et al., 1994; Weedon and

Strutton, 1981; Botchkareva et al., 2006; Matsuo et al., 1998). During catagen, distinct HF compartments produce factors that either activate or inhibit apoptosis (Lindner et al., 1997; Müller-Röver et al., 1999; Botchkareva et al., 2006; Müller-Röver et al., 2000; Rückert et al., 2000), as well as factors that terminate pro-proliferation signaling (Hsu et al., 2011; Botchkareva et al., 2006). For example, cells could exchange apoptosis-activating signals, including the *Tumor Necrosis Factor* (Tnf) which contributes to its wave-like propagation (Eroglu and Derry, 2016; Pérez-Garijo et al., 2013). On the other hand, DP cells do not undergo apoptosis, but move upward following the shrinking epithelium until the HF returns to its minimal structure, marking the entering of telogen. (Hsu and Fuchs, 2012; Botchkareva et al., 2006; Matsuo et al., 1998; Stenn et al., 1994; Stenn, 1998; Soma et al., 1998; Heitman et al., 2020; Martino et al., 2021). Catagen typically lasts for about 2–3 weeks in humans and for 3 days in mice (Straile et al., 1961; Kligman, 1959; Parakkal, 1970).

While the anagen-to-catagen degeneration is irreversible, recent experimental studies revealed that HFs exhibit regenerative dynamics when follicle damage is induced by ionizing radiation (IR) at the mature anagen stage (Huang et al., 2017, 2019). It is observed that when weak IR is applied, a HF experiences minor length shrinkage then returns to its homeostatic state, compared to application of strong radiation where a major HF involution accompanied by a high level of apoptosis occurs, yet the HF is still able to regenerate and return to its normal homeostatic state. Both regenerative dynamics – after weak and strong IR – are essentially different from the normal progressive, irreversible degeneration during catagen. This gives rise to critical questions related to HF regeneration control: while both degenerative dynamics start with massive apoptosis, why is the degeneration during catagen irreversible while the IR induced (anagen) degeneration is transient and followed by regeneration? Are the mechanisms underlying these degenerative dynamics essentially different?

In recent years, the HF system has caught the interests of many modeling groups, and there are several modeling works dedicated to the study of HF growth control mechanisms and cell fate regulations (Halloy et al., 2000; Plikus et al., 2011; Al-Nuaimi et al., 2012; Murray et al., 2012; Wang et al., 2017; Zamil et al., 2021; Dinh and Wang, 2022). We also refer the reader to Painter et al. (2012, 2021) for a recent review of modeling studies in HF morphogenesis. The goal of this paper is to develop a HF cell differentiation population model, and use it to investigate the underlying mechanisms behind the IR induced HF regenerative dynamics and compare to those that drive the catagen degenerative dynamics. That is, we focus on the instant dynamic behaviors after a one-time application of IR or at the anagen-to-catagen transition. This paper is organized as follows. In Section 2, we develop the HF model following the classic cell differentiation population model framework and based on currently known HF biology from literature. In Section 3, we first calibrate the model parameters using experimental data, then in Section 4 we apply stability, bifurcation and sensitivity analyses to the system to identify the key factors that regulate IR-induced HF regeneration or anagen-to-catagen degeneration (Sections 4.1, 4.2).

2. A cell differentiation population ODE model of hair follicle dynamics

We first develop a new ODE model that focuses on the local dynamics of the bottom part of the HF, which is the dynamic portion of the HF during anagen. While some biological details of the HF growth cycle have been presented in the Introduction section, here we briefly reiterate them, and expand upon additional mechanisms based on which we develop the model.

2.1. Summarized HF biology and model assumptions

During anagen, the bottom part of a HF mainly consists of three functional components: the DP, the Mx and the active portion of ORS (Fig. 1B) ; apoptosis cells may arise from the two latter epithelial compartments.

- The DP is a cluster of specialized fibroblasts that actively participate in the HF signaling dynamics. It interacts with Mx and *active* ORS (see explanations below for ORS) through various signaling pathways that help regulate Mx and ORS cell division and differentiation. In our model we consider these signals as background regulators and, since DP cells do not divide or undergo cell death, we do not explicitly include the DP in the dynamics of our model. Instead, we consider the DP as dynamically stable.
- ORS are epithelial cells derived mostly from the bulge stem cells; they form the outer epithelial layer of the HF. At the base of the HF, ORS cells connect with and can differentiate into Mx cells. In our model, we roughly divide ORS into two sub-parts: the dynamic part of ORS at the bottom of the HF, referred to as the *active* ORS (denoted as ORS_a in our model), and the rest of the ORS referred to as the *quiescent* ORS (denoted as ORS_q), which are away from the DP signaling center and do not actively divide during most of anagen.
- Mx cells are a group of epithelial transient amplifying cells, they divide fast and give rise to several types of terminally differentiated cells including HS and IRS. When Mx cells run out of dividing potential, they start apoptotic death. During anagen, Mx cells produce signals such as Wnt and Shh that activate ORS cell divisions —in the model we denote these signals as signal B (Fig. 2A).
- During anagen there are only very few apoptotic cells, yet upon the anagen-to-catagen transition, a coordinated apoptotic wave originates in the Mx and propagates upward thanks to the exchange of apoptosis-activating signals, such as Tnf. We model these signaling dynamics in a way that cells under-going apoptosis, represented as Apop cells, produce an apoptosis-activating signal A to activate further apoptosis in neighboring Mx and ORS cells.

The cell differentiation relations and the feedback controls at the bottom part of a HF in our model are illustrated in Fig. 2.

2.2. HF cell differentiation population model

We develop a new cell population model for HF regeneration following the classic cell differentiation population ODE modeling framework (Lo et al., 2009; Lander et al., 2009;

Doumic et al., 2011; Marciniak-Czochra et al., 2009), shown by Eq. (1) and described in detail as follows as well as in Appendix A.

$$\frac{d[\mathrm{ORS}_q]}{dt} = -f([\mathrm{ORS}_a]) \tag{1a}$$

$$\frac{d[\mathrm{ORS}_a]}{dt} = f([\mathrm{ORS}_a]) + (2p^p_{\mathrm{ORS}} - 1)\nu_{\mathrm{ORS}}[\mathrm{ORS}_a] \tag{1b}$$

$$\frac{d[\mathrm{Mx}]}{dt} = 2p^d_{\mathrm{ORS}}\nu_{\mathrm{ORS}_a}[\mathrm{ORS}_a] + (2p^p_{\mathrm{Mx}} - 1)\nu_{\mathrm{Mx}}[\mathrm{Mx}] \tag{1c}$$

$$\frac{d[\mathrm{Apop}]}{dt} = p^a_{\mathrm{ORS}}\nu_{\mathrm{ORS}_a}[\mathrm{ORS}_a] + p^a_{\mathrm{Mx}}\nu_{\mathrm{Mx}}[\mathrm{Mx}] - d[\mathrm{Apop}] \tag{1d}$$

where ORS_q and ORS_a denote quiescent and active ORS cells, respectively, Mx denotes hair matrix cells and Apop represents cells under-going apoptosis. In Eqs. (1), $[\cdot]$ denotes the size of a certain type of cell. Since we do not consider spatial information in the HF system, $[\cdot]$ can be equivalently considered as the cell concentration, which is the usual meaning in cell population models.

The expressions p^p_{ORS}, p^p_{Mx} denote the proliferation rates of ORS and Mx cells, respectively; p^d_{ORS}, p^d_{Mx} denote the differentiation rates of ORS and Mx cells, respectively; and p^a_{ORS}, p^a_{Mx} the apoptosis rates of ORS and Mx cells, respectively. Notice that p^d_{Mx} does not explicitly appear in the system, rather it plays an implicit role since we impose that these rate functions should satisfy the following constraints:

$$p^p_{\mathrm{ORS}} + p^d_{\mathrm{ORS}} + p^a_{\mathrm{ORS}} = 1 \tag{2a}$$

$$p^p_{\mathrm{Mx}} + p^d_{\mathrm{Mx}} + p^a_{\mathrm{Mx}} = 1 \tag{2b}$$

ν_{ORS}, ν_{Mx} are the dividing frequencies of ORS and Mx cells, which relate to the cell cycle time T by the relation $\nu = \ln 2 / T$. The average cell cycle time of Mx cells in mice is ~ 12 h (Stenn and Paus, 2001; Malkinson and Keane, 1978), in our model we take this as 1 computational time unit, i.e., $T = 1$ is equivalent to 12 h, and we have $\nu_{\mathrm{Mx}} = \ln 2$. d is the degradation rate of apoptosis cells, that is, the rate at which they exit the system. The function $f([\mathrm{ORS}_a])$ describes the transition between the quiescent ORS and active ORS cells, and we assume the following simple form of f:

$$f([\mathrm{ORS}_a]) = h_{\mathrm{ORS}}(C_{\mathrm{ORS}} - [\mathrm{ORS}_a]) \tag{3}$$

where C_{ORS} stands for the equilibrium size of active ORS cells, and h_{ORS} is the transition rate.

The feedback controls are modeled as follows. Apop cells may produce signals to activate apoptosis in ORS_a, and Mx cells, we assume that the apoptosis rates of ORS and Mx cells p^a_{ORS}, p^a_{Mx} depend on the size of Apop cells via the following Hill-function type of controls:

$$p^a_{\mathrm{ORS}}([\mathrm{Apop}]) = p_2\left[s_2 + \frac{\alpha_2[\mathrm{Apop}]^{n_2}}{1+\alpha_2[\mathrm{Apop}]^{n_2}}\right] \tag{4a}$$

$$p^a_{\mathrm{Mx}}([\mathrm{Apop}]) = p_3\left[s_3 + \frac{\alpha_3[\mathrm{Apop}]^{n_3}}{1+\alpha_3[\mathrm{Apop}]^{n_3}}\right] \tag{4b}$$

Mx cells may produce signal A that activates ORS_a cells' proliferation, thus we assume that the ORS_a proliferation rate, p^p_{ORS} depends on the size of Mx cells:

$$\begin{aligned} p^p_{\mathrm{ORS}}([\mathrm{Mx}],[\mathrm{Apop}],[\mathrm{ORS}_q]) &= (1-p^a_{\mathrm{ORS}}([\mathrm{Apop}])) \\ &\times g([\mathrm{ORS}_q])p_1\frac{\alpha_1[\mathrm{Mx}]^{n_1}}{1+\alpha_1[\mathrm{Mx}]^{n_1}} \end{aligned} \tag{5}$$

where we include an additional control function g to describe the control of the HF length. The functional forms of Eqs. (4a) (4b) and (5) are illustrated in Fig. E.15 using calibrated parameter values (Table E.2). Finally, all probability functions (p's) in our model are forced to be bounded between 0 and 1.

On the control function g.—HFs grow during the early stage of anagen until they reach their maximum length, then they stop further downward growth but keep producing hair shaft. Up to date, the mechanisms that determine the HFs' maximum length and maintain their homeostasis are still unclear. An intuitive guess would be that there might be some signal X produced by Mx cells that inhibits ORS cell proliferation, so that when the HF reaches its maximum size, the ORS cell proliferation is greatly inhibited by this signal, allowing the HF to stay at that length. However, to our knowledge, no such signal X has been identified. Due to the lack of further evidence on the HF length control mechanism, in our model, we include this control as a function g in the ORS cell proliferation rate p^p_{ORS}. Moreover, we would like to emphasize that the feedback mechanism from Mx to ORS cells through signal B serves to activate instead of to inhibit ORS cell proliferation.

We use the size of quiescent ORS as a rough measure of the HF length, and phenomenologically model the length control in the following way:

$$g([\mathrm{ORS}_q]) = \frac{E_q}{[\mathrm{ORS}_q]} \tag{6}$$

where E_q represents the equilibrium size of quiescent ORS cells $[\mathrm{ORS}_q]$. We point out that without the HF length control, i.e. $g \equiv 1$, Eqs. (1b) (1c) (1d) will form a closed system of $[\mathrm{ORS}_a]$, [Mx], [Apop], while $[\mathrm{ORS}_q]$ can be considered as an output of the subsystem (Eqs. (1b) (1c) (1d)) by Eq. (1a). In this case, it is easy to see the following:

Lemma 1. *If* $\overline{[ORS_q]}, \overline{[ORS_a]}, \overline{[Mx]}, \overline{[Apop]}$ *is an equilibrium state of the system* (1) *with* $g \equiv 1$*, then for any c such that* $\overline{[ORS_q]} + c \geq 0$, $(\overline{[ORS_q]} + c, \overline{[ORS_a]}, \overline{[Mx]}, \overline{[Apop]})$ *is also an equilibrium state.*

Proof. With $g \equiv 1$, the equation system (1) can be written as

$$\frac{d[\mathrm{ORS}_q]}{dt} = \phi_1([\mathrm{ORS}_a]) \tag{7a}$$

$$\frac{d[\mathrm{ORS}_a]}{dt} = \phi_2([\mathrm{ORS}_a], [\mathrm{Mx}], [\mathrm{Apop}]) \tag{7b}$$

$$\frac{d[\mathrm{Mx}]}{dt} = \phi_3([\mathrm{ORS}_a], [\mathrm{Mx}], [\mathrm{Apop}]) \tag{7c}$$

$$\frac{d[\mathrm{Apop}]}{dt} = \phi_4([\mathrm{ORS}_a], [\mathrm{Mx}], [\mathrm{Apop}]) \tag{7d}$$

If $(\overline{[\mathrm{ORS}_q]}, \overline{[\mathrm{ORS}_a]}, \overline{[\mathrm{Mx}]}, \overline{[\mathrm{Apop}]})$ is an equilibrium state of the system (7), then

$$\Phi(\overline{[\mathrm{ORS}_q]}, \overline{[\mathrm{ORS}_a]}, \overline{[\mathrm{Mx}]}, \overline{[\mathrm{Apop}]}) = \vec{0} \tag{8}$$

where $\Phi = (\phi_1, \phi_2, \phi_3, \phi_4)^T$. Since the ϕ_i, $i = 1, \ldots, 4$ do not depend on $[\mathrm{ORS}_q]$, we can write Eq. (8) as

$$\Phi(\overline{[\mathrm{ORS}_a]}, \overline{[\mathrm{Mx}]}, \overline{[\mathrm{Apop}]}) = \vec{0}$$

Therefore, for any constant c such that $\overline{[\mathrm{ORS}_q]} + c \geq 0$, we have

$$\Phi(\overline{[\mathrm{ORS}_q]} + c, \overline{[\mathrm{ORS}_a]}, \overline{[\mathrm{Mx}]}, \overline{[\mathrm{Apop}]}) = \Phi(\overline{[\mathrm{ORS}_a]}, \overline{[\mathrm{Mx}]}, \overline{[\mathrm{Apop}]}) = 0$$

which indicates that $(\overline{[\mathrm{ORS}_q]} + c, \overline{[\mathrm{ORS}_a]}, \overline{[\mathrm{Mx}]}, \overline{[\mathrm{Apop}]})$ is also an equilibrium state of the system (7). □

The above Lemma indicates that if $g \equiv 1$, then any constant value of the ORS_q compartment size is an equilibrium of the HF model. This violates the biological fact that the homeostatic HF length (roughly represented by size of $[\mathrm{ORS}_q]$) during anagen is well determined. This shows that a growth control mechanism that possibly depends on the HF length, or equivalently, the size of ORS_q in our model is necessary for the HF system.

2.3. Modeling of ionizing radiation (IR) induced HF regeneration

In the experimental study from Huang et al. (2017), different strength of IR (2 Gy and 5.5 Gy) is applied to mouse HFs, and the effects are observed and analyzed in the following days. In Huang et al. (2017) (also see Fig. 3), proliferative Mx cells are identified as

$BrdUrd^+$ Mx cells. The study finds that there are no $BrdUrd^+$ Mx cells detected at 6 h post-exposure of either 2 Gy or 5.5 Gy IR, effectively causing a pause in the Mx cellular processes, thus we can interpret this as Mx cells entirely being affected by IR as follows. We assume that during $t < 0$, the system (1) is at equilibrium, corresponding to the homeostatic state in non-radiated, or controlled, mouse HFs. At $t = 0$, we introduce in a new quantity Mx^{IR} denoting the Mx cells that pause their cellular processes due to IR exposure, and we assume that at $t = 0$, all current Mx cells become Mx^{IR}, i.e.,

$$\text{Simulated IR exposure:} \quad [\mathrm{Mx}^{\mathrm{IR}}](0) = \lim_{t \to 0^-} [\mathrm{Mx}](t), \qquad [\mathrm{Mx}](0) = 0$$

Also according to Huang et al. (2017), after IR exposure, Mx cells eventually restart their cellular processes including both cell proliferation and apoptosis, and there is an inflow of ORS cells into the hair bulb to replenish the Mx cell population. Thus, we assume that after the simulated IR exposure, Mx^{IR} cells can either return to normal Mx cells at a rate of q, or they can start apoptosis at the rate of $1 - q$. The dynamics of the Mx^{IR} are described by the following equations, and illustrated in Fig. 2B.

$$\frac{d[\mathrm{Mx}^{\mathrm{IR}}]}{dt} = -\gamma[\mathrm{Mx}^{\mathrm{IR}}] \tag{9a}$$

$$\frac{d[\mathrm{Mx}]}{dt} = \gamma q[\mathrm{Mx}^{\mathrm{IR}}] + 2p^{d}_{\mathrm{ORS}}\nu_{\mathrm{ORS}_a}[\mathrm{ORS}_a] + (2p^{p}_{\mathrm{Mx}} - 1)\nu_{\mathrm{Mx}}[\mathrm{Mx}] \tag{9b}$$

$$\frac{d[\mathrm{Apop}]}{dt} = \gamma(1-q)[\mathrm{Mx}^{\mathrm{IR}}] + p^{a}_{\mathrm{ORS}}\nu_{\mathrm{ORS}_a}[\mathrm{ORS}_a] + p^{a}_{\mathrm{Mx}}\nu_{\mathrm{Mx}}[\mathrm{Mx}] - d[\mathrm{Apop}] \tag{9c}$$

γ is the "degradation" rate of Mx^{IR}, which can be understood as the rate at which the Mx^{IR} cells quit their interrupted state, and Eqs. (9b) (9c) are modified from Eqs. (1c) (1d) to include the post-radiation transitions of Mx^{IR} just described. That is, return to normal ($\gamma q[\mathrm{Mx}^{\mathrm{IR}}]$ in Eq. (9b)), or start apoptosis ($\gamma(1-q)[\mathrm{Mx}^{\mathrm{IR}}]$ in Eq. (9c)).

2.4. Modeling of Mx cells' lineage tracing after IR

In the 1R simulations, we are also interested in how much the ORS-to-Mx differentiation contributes to the Mx regeneration, therefore we would like to inspect the post-radiation Mx lineage tracing. At $t = 0$, all current Mx cells turn into Mx^{IR}. For $t > 0$, we mark the Mx cells derived from ORS cells and their progeny cells as Mx+, and those that recover from Mx^{IR} as Mx−. The dynamics of [Mx] in Eq. (9) are further decomposed into the following two equations:

$$\frac{d[\mathrm{Mx}+]}{dt} = 2p^{d}_{\mathrm{ORS}}\nu_{\mathrm{ORS}_a}[\mathrm{ORS}_a] + (2p^{p}_{\mathrm{Mx}} - 1)\nu_{\mathrm{Mx}}[\mathrm{Mx}+] \tag{10a}$$

$$\frac{d[\mathrm{Mx}-]}{dt} = \gamma q[\mathrm{Mx}^{\mathrm{IR}}] + (2p^{p}_{\mathrm{Mx}} - 1)\nu_{\mathrm{Mx}}[\mathrm{Mx}-] \tag{10b}$$

where $[\mathrm{Mx}+] + [\mathrm{Mx}-] = [\mathrm{Mx}]$ gives the total Mx cell population.

2.5. Stochastic model

The ODE model developed above allows us to study the average population dynamics of different HF compartments, as well as performing stability and bifurcation analysis on the system, which helps us understand the key factors regulating the HF regenerative dynamics from a deterministic point of view. However, it has two major limitations:

1. The compartments in a real HF usually have a relatively low number of cells, typically of the orders from $O(1) - O(10^2)$. For such small-sized compartments and systems, it is known that stochastic effects may become important and cannot be captured in a deterministic population model, which usually assumes a high number of population so that the average population dynamics dominates over the stochastic effects.
2. Our ODE model assumes cell number varies continuously in the region $[0, +\infty)$, while in reality, cell numbers should be non-zero integers $\mathbb{Z}^+ \cup \{0\}$.

Therefore, to supplement our ODE model and to further investigate the stochastic behaviors in the HF system, we develop the associated stochastic model. While the stochastic model was originally developed for chemical reactions, modeling studies of cell lineage dynamics have also borrowed this framework (Sun et al., 2016). The general idea is describing a cellular process as a reaction, for example, the ORS_a proliferation (Fig. 2) can be written as the following reaction equation:

$$\mathrm{ORS}_a \rightarrow 2\mathrm{ORS}_a$$

This reaction happens at the rate of $\nu_{\mathrm{ORS}}p^{p}_{\mathrm{ORS}}(t)[\mathrm{ORS}_a](t)$, where again $[\mathrm{ORS}_a](t)$ denotes the current ORS_a cell number, though in the stochastic model it takes values in $\mathbb{Z}^+ \cup \{0\}$, and $p^{p}_{\mathrm{ORS}}(t)$ is the current ORS_a proliferation rate as defined in Eq. (5); when this reaction happens, it will lead to ORS_a cell number increased by 1 cell, while all other cell types in the system do not change their cell numbers.

In Table E.1 we provide more details of the reactions in the stochastic model. We use Gillespie's direct method (Gillespie et al., 2007) to perform the stochastic simulations.

3. Model parameters

In this section, we derive additional constraints using relations obtained from the steady state of system (1) which corresponds to the non-radiated, or control case in mice from

experimental study (Huang et al., 2017). We then summarize the main findings in the same work, and use their experimental data to calibrate the parameters in our HF model. Lastly, we show simulation results using the parameter set obtained from the calibration.

3.1. Information from control case

In the control case, or equivalently, 0 Gy IR, apoptosis is hardly detected during anagen until the initiation of catagen. Therefore, $[\text{Apop}] \equiv 0$, $p^a_{\text{ORS}} = p^a_{\text{Mx}} = 0$ in the system without IR exposure (Eqs. (1)), and Eqs. (4) give

$$p^a_{\text{ORS}}([\text{Apop}] = 0) = p_2 s_2 = 0, \quad p^a_{\text{Mx}}([\text{Apop}] = 0) = p_3 s_3 = 0$$

Since p_2, p_3 cannot be zero otherwise the feedback controls from Apop to Mx and ORS_a will be trivially zero (Eqs. (4)), the above relations indicate that $s_2 = s_3 = 0$. That is, the spontaneous apoptosis rates in Mx and ORS cells during anagen are both zero.

Without radiation exposure, HF growth should stay homeostatic during anagen, thus the system (1) should stay in its equilibrium state. We have discussed above that at the equilibrium state, [Apop] = 0. Furthermore, we use data from Huang et al. (2017) to estimate the equilibrium size of Mx, denoted E_{Mx}, by extracting the control average value of Mx, which gives $E_{\text{Mx}} \approx 128$. There is no direct clue from the data about the equilibrium values of $[\text{ORS}_q]$ and $[\text{ORS}_a]$, yet from system (1),

$$\frac{d[\text{ORS}_q]}{dt} = f([\text{ORS}_a]) = h_{\text{ORS}}(C_{\text{ORS}} - [\text{ORS}_a]) = 0$$

thus we should have $[\text{ORS}_a] = C_{\text{ORS}}$. Finally, considering the length control function g (Eq. (6)), we take $[\text{ORS}_q] = E_q$ as the equilibrium value. Therefore, we obtain the equilibrium state in HF growth dynamics system (1):

$$(\overline{[\text{ORS}_q]}, \overline{[\text{ORS}_a]}, \overline{[\text{Mx}]}, \overline{[\text{Apop}]}) = (E_q, C_{\text{ORS}}, E_{\text{Mx}}, 0)$$

where $E_{\text{Mx}} \approx 128$, while the values of E_q and C_{ORS} are to be determined.

Two other constraints for the parameters can be obtained by the steady state of the system (1). At the steady state, Eqs. (1b) (1c) can be reduced to

$$\frac{d[\text{ORS}_a]}{dt} = (2p^p_{\text{ORS}} - 1)\nu_{\text{ORS}}[\text{ORS}_a] = 0$$
$$\frac{d[\text{Mx}]}{dt} = 2p^d_{\text{ORS}}\nu_{\text{ORS}}[\text{ORS}_a] + (2p^p_{\text{Mx}} - 1)\nu_{\text{Mx}}[\text{Mx}] = 0$$

with

$$p^p_{\text{ORS}} = p_1 \frac{\alpha_1 E^{n_1}_{\text{Mx}}}{1 + \alpha_1 E^{n_1}_{\text{Mx}}}, \quad p^p_{\text{ORS}} + p^d_{\text{ORS}} = 1, \quad p^p_{\text{Mx}} + p^d_{\text{Mx}} = 1$$

From the above relations, we obtain the following constraints at the equilibrium:

$$p_1 \frac{\alpha_1 E_{\mathrm{Mx}}^{n_1}}{1+\alpha_1 E_{\mathrm{Mx}}^{n_1}} = \frac{1}{2} \tag{11a}$$

$$p_{\mathrm{Mx}}^{p} = \frac{1}{2}\left(1 - \frac{\nu_{\mathrm{ORS}} C_{\mathrm{ORS}}}{\nu_{Mx} E_{Mx}}\right) \in \left[0, \frac{1}{2}\right] \tag{11b}$$

Notice that we did not specify any conditions between the proliferation and differentiation rates of Mx cells, i.e., p_{Mx}^{p}, p_{Mx}^{d} in Eq. (2b). Published studies suggest that Mx cells mostly respond to both proliferation (including Fgf7/10) and differentiation signals (including Bmp and its antagonist Noggin) sent from the DP (Paus and Foitzik, 2004; Hsu et al., 2014; Millar, 2002; Hsu and Fuchs, 2012; Rezza et al., 2016; Kulessa et al., 2000; Takahashi and Ikeda, 1996; Yang and Cotsarelis, 2010; Sennett and Rendl, 2012; Rendl et al., 2008; Kobielak et al., 2003; Driskell et al., 2011; Botchkarev and Kishimoto, 2003; Botchkarev, 2003; Botchkarev et al., 1999), and that Bmp ligands might have a longer effective range than Fgf and Noggin ligands, which results in an upward-oriented pro-proliferation-to-pro-differentiation signaling gradient (Takahashi and Ikeda, 1996). Since the DP is relatively stable, we assume that such a pro-proliferation-to-pro-differentiation signaling gradient imposed on Mx is also stable, from which we may assume that $p_{\mathrm{Mx}}^{p} / p_{\mathrm{Mx}}^{d}$ keeps the same ratio during anagen. Therefore, we take the value from Eq. (11b) as r, and assume the following relations for Mx cells:

$$r = \frac{1}{2}\left(1 - \frac{\nu_{\mathrm{ORS}} C_{\mathrm{ORS}}}{\nu_{Mx} E_{Mx}}\right), \quad p_{\mathrm{Mx}}^{p} = r(1 - p_{\mathrm{Mx}}^{a}), \quad p_{\mathrm{Mx}}^{d} = (1-r)(1 - p_{\mathrm{Mx}}^{a}) \tag{12}$$

Finally, we point out that studies also show that there are other dynamic supplementary resources for Bmp ligands that promote Mx cell differentiation, which may include ORS and another group of transient amplifying cells derived directly from Mx, called precortex (Takahashi and Ikeda, 1996; Blessing et al., 1993). However, considering that the DP serves as the main source of Mx cell proliferation and differentiation signals, for now we do not consider these additional sources in our model and adopt the simplified assumption (Eqs. (12)).

3.2. Calibration of parameters using experimental data

With all above considerations, we calibrate our model parameters to data from Huang et al. (2017).

3.2.1. Summary of the major discoveries from the IR experimental results—

We first summarize the major discoveries about IR induced HF regenerative dynamics from Huang et al. (2017), listed below:

- IR is applied to two distinct groups of mice; one is applied IR of strength 2 Gy, and the other a strength of 5.5 Gy. Through staining techniques, researchers from Huang et al. (2017) are able to quantify the number of proliferative cells, the

percent of apoptotic cells in the matrix, the HF length, as well as the tracking of Mx cells lineage post-radiation.

- *Apoptotic Mx cells.* With either 2 or 5.5 Gy IR, apoptosis is detected in Mx cells shortly after exposure during (0–6 h) (referred to as $TUNEL^+$ Mx cells in Huang et al. (2017)). With 2 Gy IR, the number of apoptotic Mx cells returns to zero at ~ 24 h; with 5.5 Gy IR, it takes until ~ 72 h for the number of apoptotic Mx cells to return to zero. See plots in Fig. 3AA′ regenerated from data from Huang et al. (2017).
- *Mx cells.* With 2 Gy IR, the number of Mx cells decreases to about half the initial number at ~ 24 h, then returns to the equilibrium level at ~ 72 h; with 5.5 Gy IR, the number of Mx cells continues to decrease until ~ 72 h, then increases from ~ 72 h to day 7, however catagen starts at day 7 before Mx is fully regenerated (Fig. 3BB′). Moreover, In both 2 Gy and 5.5 Gy IR, no proliferating Mx cells (referred to as $BrdUrd^+$ in Huang et al. (2017)) are detected at 6 h. After that, with 2 Gy IR, the number of proliferating Mx cells increases significantly until ~ 48 h after which point it remains at more or less the same level until day 7; with 5.5 Gy IR, the number of proliferating Mx cells shows a slight recovery and stays at a low level during 6–72 h, then it returns to zero at 72 h, followed by a second recovery attempt until day 7, referred to as *the second regeneration attempt* (Fig. B.12BB′).
- *HF length.* With 2 Gy IR, there is a small decrease in the HF length with minimum occurring at ~ 48 h before returning to a normal level; with 5.5 Gy IR, the HF shrinks significantly to about half the original length by 72 h then returns to normal by day 7 (Fig. 3CC′). In both cases the HF length is fully regenerated by day 7, when catagen starts.
- *ORS to Mx flow.* In normal HFs, keratin 5 (K5+) is present exclusively in cells in the basal area of the hair bulb. With 2 Gy or 5.5 Gy IR, K5+ is found in cells upwards of the basal area, indicating that these cells contribute to the bulb regeneration.

3.2.2. Parameter calibration—First, we note that from the biological point of view, it would be suspicious to calibrate all parameters separately to the 2 Gy dataset and 5.5 Gy dataset, though mathematically the results would look better. For the parameters in our model system, some of them are closely related to IR strength and apoptosis signaling dynamics, while others are not. Therefore, we divide the parameters into the two groups:

$$\text{Group 1:} \quad \gamma, q, \alpha_2, \alpha_3, p_2, p_3, s_2, s_3, n_2, n_3, d \tag{13a}$$

$$\text{Group 2:} \quad h_{\text{ORS}}, C_{\text{ORS}}, \nu_{\text{ORS}}, \nu_{\text{Mx}}, p_1, \alpha_1, n_1, E_q, E_{\text{Mx}} \tag{13b}$$

Group 1 parameters either directly relate to IR (γ, q) or they participate in the apoptosis signaling pathway ($\alpha_2, \alpha_3, p_2, p_3, s_2, s_3, n_2, n_3, d$). Group 2 includes all other parameters. The

parameter $\nu_{Mx} = \ln 2$, and we have determined $s_2 = s_3 = 0$, $E_{Mx} = 128$ as discussed in Section 3.1. We further assume that the Hill exponents $n_1 = n_2 = n_3 = 2$ for simplicity. For other parameters, we impose that group 2 parameters should have the same value despite of IR strength, while group 1 parameters can be selectively different depending on IR strength.

We first tried to use the least square method by creating an optimization problem using Matlab functions `fcn2optimexpr` and `optimproblem`. The data to be fitted are 2 Gy and 5.5 Gy data of apoptosis Mx cells (Fig. 3AA′ blue boxes), bulb cells (Fig. 3BB′ blue boxes) and the percentage of HF length (Fig. 3CC′ blue boxes), at time points hour 0, 6, 12, day 1, 1.5, 2, 3, 4, 5 and 7. We use the same parameters from group 2 (13b) for both 2 Gy and 5.5 Gy data, while parameters from group 1 (13b) are allowed to be different to fit separately to the 2 Gy and 5.5 Gy data. Initial guesses of the parameter values are randomly chosen. Unfortunately, the better results from the least square method give parameters that predict biologically unrealistic dynamics when observing the long-term behavior after the last experimental observation at time point (day 7): for example, some of the results do not show the HF regeneration observed in the 5.5 Gy IR experiments, or some others show large amplitude of oscillations in HF length. Therefore, instead of seeking the optimal fitted parameter values, we chose a set of parameter values that numerically matches the experimental data to a reasonable extent, while remaining biologically meaningful and captures the major characteristic behaviors in IR induced HF regeneration.

The calibrated parameter values are given in Table E.2, where altogether we have 18 free variables, with p_2, p_3, α_2, α_3, q having separate values for 2 Gy and 5.5 Gy data. s_2, s_3, ν_{Mx}, E_{Mx} are predetermined from literature thus are not included in these 18 free variables. The simulation results with the calibrated parameter values are shown in Fig. 3AA′BB′CC′ by the red solid lines, in comparison to the IR experiment data shown by the blue boxes.

Comparing simulation results with the IR experimental data, we find that apoptotic Mx cell number and bulb cell number show good agreement with the data (Fig. 3AA′BB′). On the other hand, there is some differences between the simulation and data of the HF length percentage. This is mostly because of the following two reasons. First, our model does not have spatial information, and the HF length is approximated as the ratio of the current number of ORS cells in the radiation systems to the number of ORS cells in the control case. Second, it is possible that the simple assumption of the HF length control function g (Eq. (6)) may lead to a slow HF regeneration, compared to the real biological HF length control mechanism. Considering these two model simplifications and that the calibrated results still capture the characteristics of the HF length regeneration dynamics, we accept this set of parameter values. From both the IR data and simulation results in Fig. 3AA′BB′CC′, we see that in either 2 Gy or 5.5 Gy case, IR induces massive apoptosis but only during the early stage. 5.5 Gy IR causes significant decrease in both bulb cells and the HF length in comparison to 2 Gy IR, yet in both cases, the HF is able to return to its homeostatic state, though the simulation predicts longer time for HF length recovery.

Finally, we also point out that another dataset at day 10 post-IR is presented in Huang et al. (2017), which clearly shows drops in both the HF length and Mx cell numbers, indicating that the HF has entered the degenerating catagen phase. Since our model does not count for

the dynamics of the whole HF growth cycle, we ignore this day 10 catagen dataset as our model cannot predict an automatic onset of catagen. We also extend most of our simulations to day 20 to better assess the long-term regenerative behavior, since, as is shown in Fig. 3A′B′C′, in the 5.5 Gy simulations it takes a longer time than 7 days for the HF to fully regenerate to a pre-IR level—this also seems to be true for the 5.5 Gy IR experiment; indeed, catagen begins after day 7 before the Mx can fully return to its pre-IR level (figure 1E from Huang et al. (2017)).

3.3. Simulation results with calibrated parameter values

In Fig. 4, we show the simulated dynamics of each HF compartment after 2 Gy or 5.5 Gy IR (Fig. 4AC), as well as sample paths from the corresponding stochastic simulations (Fig. 4BD). The deterministic and stochastic simulations show similar regenerative dynamic patterns. After IR exposure, a wave of apoptosis cells is triggered but quickly goes away (black solid lines). The radiated Mx cells (Mx^{IR}) also quickly disappear from the system (magenta dashed lines); while the regular Mx compartment (magenta solid lines) quickly regenerates in the 2 Gy IR simulation (4AB), while in the 5.5 Gy IR simulation, the regular Mx compartment first regenerates quickly, is followed by another drop, then regenerates again (4CD). For ORS, we notice that the ORS_a compartment mostly maintains its size despite the IR (blue solid lines); while ORS_q relatively maintains its regular size in the 2 Gy IR simulation (4AB), indicating little change in the HF length, yet in the 5.5 Gy IR simulation, a clear drop in the ORS_q size is observed, followed by a slow regeneration, which indicates an early degenerating HF followed by a regeneration. Comparing the 2 Gy vs. 5.5 Gy IR simulations, we find that while all HF compartments regenerate relatively quickly in the 2 Gy IR simulations, it takes much longer to regenerate in the 5.5 Gy IR simulations, especially for Mx and ORS_q. The slow regeneration of the Mx compartment predicted from our 5.5 Gy IR simulations seems to coincide with that shown by the 5.5 Gy IR experiment (figure 1E from Huang et al. (2017)), although the experiment shows a faster regeneration in the HF length. Comparing the deterministic ODE model simulations (4AC) with the corresponding stochastic simulations (4BD), we find that the Mx compartment size shows a larger variance thus is more dynamic compared to other compartments, while ORS_a shows a small variance.

In Appendix B, we discuss further comparisons between model and experimental data for proliferating Mx cells and the ORS-to-Mx differentiation lineage dynamics. In Appendix C, we present and discuss the posterior distributions of the model parameters.

4. Results

4.1. During anagen, the homeostatic state of anagen HF is stable, and does not depend on the apoptosis feedback strength

The major goal of this modeling research is to understand the control mechanisms of the HF regenerative dynamics. In particular, why is the HF able to regenerate itself from the IR induced degeneration during anagen, but cannot stop the progressive degeneration during catagen? In this part, we apply linear stability analysis and sensitivity analysis to address this question.

4.1.1. Linear stability analysis—In our model, several parameters are identified as directly related to the IR and apoptosis dynamics (group 1 from Eq. (13a)). Within these parameters, γ and q depend on the IR strength, Hill exponents n_2 and n_3 are assumed to be a constant, d is the "death" rate of apoptosis cells—the rate at which they quit the system, and usually such a rate is considered to be stable. This leaves six other parameters in this group: the spontaneous apoptosis rates in ORS and Mx cells – s_2, s_3, and the Apop-to-ORS, Apop-to-Mx feedbacks strength – α_2, p_2, α_3, p_3 that control the coordinated apoptosis dynamics in ORS and Mx. In controlled mice, during anagen, spontaneous apoptosis in the HF epithelium is hardly detected, as is reported in Huang et al. (2017). Based on this observation, we set the spontaneous apoptosis rates in ORS and Mx, $s_2 = s_3 = 0$ as discussed in Section 3.1. Furthermore, the anagen HF homeostasis is characterized by the steady state (E_q, C_{ORS}, E_{Mx}, 0) in our model, as discussed above. Interestingly, linear stability analysis reveals the following result:

Lemma 2. *During anagen with* $s_2 = s_3 = 0$, *the homeostatic state* (E_q, C_{ORS}, E_{Mx}, 0) *is stable, and the stability does not depend on the apoptosis feedback strength parameters* α_2, p_2, α_3, p_3.

The proof is given in Appendix D. This Lemma explains the highly regenerative ability of the HF during anagen, even when subject to high strength of IR. Since the anagen homeostasis is stable and presumably the IR only affects the apoptosis events, the system is able to return to the homeostatic steady state despite strong IR, or equivalently, large α_2, p_2, α_3, p_3 values.

4.1.2. Local sensitivity analysis—To further understand the effects of each parameter on the HF regenerative dynamics, we perform both local and global sensitivity analysis in this and the next parts.

For the local sensitivity analysis, we use the one-factor-at-a-time (OFAT) method, that is, changing the value of a particular parameter within a range while keeping the other parameter values fixed. For each parameter, we take the parameter values ranged from 0.5 to 1.5 folds, centered at the calibrated value, and we compare the numerical results of the number of quiescent ORS cells (ORS_q) at day 20, since the number of ORS_q long after application of IR can reflect the HF's ability of regeneration. The parameter sensitivity results from controlled mice (0 Gy IR, no radiation), 2 Gy and 5.5 Gy IR simulations are shown in Fig. 5, where in the 0 Gy simulations (Fig. 5A) we also use the calibrated values of α_2, p_2, α_3, p_3 from the 2 Gy IR data. First, as is already shown by the stability analysis, the HF homeostatic state does not depend on the apoptosis feedback strength parameters α_2, p_2, α_3, p_3, and the size of ORS_q does not change (Fig. 5A). Next, the 0 Gy system is very sensitive to the parameters p_1, α_1, $\mathrm{ORS}_{\max}$, where $\mathrm{ORS}_{\max}$ is defined as $\mathrm{ORS}_{\max} = E_q + C_{\mathrm{ORS}}$, the total number of ORS cells at homeostasis in controlled mice. Decreasing the values of these parameters will greatly inhibit the HF regeneration ability (Fig. 5A). The 0 Gy system is also sensitive to C_{ORS}. Notice that these parameters directly relate to ORS cell proliferation, thus our results imply that during anagen when spontaneous apoptosis is at a very low level, the regenerative ability of the HF highly depends on its ORS cell proliferation and less on the apoptosis dynamics control. In particular, the sensitivity on p_1, α_1 should be easy to understand, as we

pointed earlier in Section 3.1, p_1 and α_1 have to satisfy the constraint Eq. (11) to keep the HF in the homeostatic state. Therefore changing only one of their values at a time will surely break homeostasis and lead to abnormal regeneration behavior of the HF.

When subjected to radiation (Fig. 5BC), first, as we pointed earlier in parameter calibration (for example, see Fig. 3C′), especially at 5.5 Gy IR, it may take >20 days for our modeled HF to fully return to the length at homeostasis, therefore all parameter values return a slightly shorter HF at day 20 (Fig. 5C). Next and more important, the system becomes sensitive to more parameters than in the controlled case. These parameters include ν_{ORS} and d, as well as p_3, α_3 which control the apoptosis feedback on Mx cells. As these parameters are varied, there is a subtle decrease in modeled HF length (ORS_q) in the 2 Gy case and a much more visible one in the 5.5 Gy case. However, no clear change in the sensitivity to the parameters controlling apoptosis feedback on ORS cells (p_2, α_2) is observed in either 2 Gy or 5.5 Gy case.

4.1.3. Global sensitivity analysis—Next, we perform a global sensitivity analysis on the parameters using the partial rank correlation coefficient (PRCC) measure (Marino et al., 2008). Latin hypercube sampling (LHS) is implemented to generate sample parameters, with parameter values uniformly distributed from 0.5 to 1.5 folds of the calibrated value. Similar to the local sensitivity analysis, we assess the number of quiescent ORS cells (ORS_q) at day 20. The PRCC results of 2 Gy and 5.5 Gy IR simulations are shown in Fig. 6, and the trajectories of the [ORS_q] from day 0 (application of the IR) to day 20 are given in Fig. E.16. In Fig. 6, the first index on the top of each panel gives the PRCC of that parameter, and the second index gives the p-value.

In 2 Gy simulations, five parameters give nearly zero p-values: p_1, α_1, C_{ORS}, ORS_{max}, q, indicating that the output ([ORS_q] at day 20) is sensitive to these parameters. Among them, four (p_1, α_1, ORS_{max}, q) show large positive PRCC measures, indicating a positive correlation between them and the output; while C_{ORS} shows a negative correlation with the output. Comparing with the local sensitivity results (Fig. 5B), the system appears to be sensitive to p_1, α_1, C_{ORS}, ORS_{max} with both local and global sensitivity analyses, while the PRCC further reveals the sensitivity on q.

In 5.5 Gy simulations, first, we notice that most parameters have smaller p-values comparing to the 2 Gy simulations, indicating that the system is more sensitive to the parameters comparing to the 2 Gy simulations—this is mostly due to that in the 5.5 Gy simulations, at day 20 the HF has not fully returned to the length at the homeostatic state, as we discussed in the local sensitivity analysis. Next, several parameters show close to 0 p-values. These are p_1, α_1, p_3, α_3, ν_{ORS}, d, C_{ORS}, ORS_{max}; they also show large, positive or negative PRCC values. We also notice that the results no longer show sensitivity to q, as in the case of 2 Gy simulations. Moreover, comparing these results with the local sensitivity results (Fig. 5B), we see that they present the same list of sensitive parameters. Among these parameters, p_1, α_1, d, ORS_{max} show positive PRCC measures, indicating positive correlations between the parameters and the output, while p_3, α_3, ν_{ORS}, C_{ORS} show negative PRCC measures thus negative correlations with the output.

4.2. Increased spontaneous apoptosis rates and strong apoptosis feedback at the anagen-to-catagen transition together result in the HF catagen degeneration

At the late stage of anagen, spontaneous apoptosis becomes prominent in Mx, which later triggers the upward propagating apoptosis wave, marking the anagen-to-catagen transition. Unlike the IR induced HF degeneration, the degeneration during catagen is irreversible and only comes to a stop when the HF enters the resting telogen phase.

In our model, the spontaneous apoptosis rate in Mx is controlled by the parameter s_3, previously set to zero to represent the absence of spontaneous apoptosis in anagen. To understand its effect, we apply bifurcation analysis with respect to s_3 on the following systems: system (1) with the 2 Gy calibrated parameter values, system (1) with the 5.5 Gy calibrated parameter values, and a few more "intermediate systems" with values of p_2, α_2, p_3, α_3 varying between the 2 Gy and 5.5 Gy calibrated values (Fig. 7, all bifurcation diagrams generated by XPPAuto, parameter values of p_2, α_2, p_3, α_3 listed in Table E.3).

First, in the 2 Gy case we observe that the stability of the steady state does not change with s_3 (Fig. 7A). Considering that the 2 Gy IR system has very weak apoptosis feedbacks on both Mx and ORS cells, determined mostly by the values of p_2, p_3 (Table E.3), this implies that increasing the spontaneous apoptosis rate (s_3) alone cannot lead to the apoptosis wave or the catagen HF degeneration. On the other hand, in the 5.5 Gy IR system (Fig. 7F), due to the strong apoptosis feedback on both ORS and Mx cells (p_2, p_3), an increase in the spontaneous apoptosis rate in Mx cell (s_3) quickly breaks down the stability of the homeostatic state: first, a Hopf bifurcation is triggered leading to a periodic solution region (Fig. 7F, green dots), followed by another stable steady state representing the degenerated HF (Fig. 7F, red solid lines).

The intermediate systems (ISs) show how the steady state evolves as the apoptosis feedbacks get stronger. With weak apoptosis feedbacks (Fig. 7BC), the steady state is able to remain stable as s_3 increases, pushing the HF system from the homeostatic state to the degenerated state. Then at a certain level of apoptosis feedback, a Hopf bifurcation occurs and a transient periodic domain shows up (Fig. 7DEF). The Hopf bifurcation is identified as subcritical, that is, an unstable periodic solution region (shown by blue circles in the close-up plot in Fig. 7D), is quickly followed by a stable periodic solution region (green dots in Fig. 7DEF). We point out that the unstable periodic-solution region is very small, and difficult to identify in XPPAuto, showing a jump from the homeostatic stable steady state to the periodic solution (Fig. 7EF).

Dynamic simulations of system (1) with 5.5 Gy calibrated parameter values p_2, α_2, p_3, α_3 and different s_3 values are shown in Fig. 8. We show simulation results from both the ODE model (8ABC) and sample paths from the corresponding stochastic simulations (8A′B′C′). In agreement with the bifurcation diagrams (Fig. 7), with $s_3 = 0$, that is, no spontaneous apoptosis in Mx cells, the HF stays in the stable homeostatic state (Fig. 8AA′). A small value of s_3 results in the degeneration of the HF, followed by periodic dynamics (Fig. 8BB′), while further increasing s_3 results in the full degeneration of the HF without showing a periodic dynamics (Fig. 8CC′), which could represent the full degeneration dynamics

during catagen. This reveals the important roles of the Mx spontaneous apoptosis rate (s_3) and the apoptosis feedback strengths (p_2, α_2, p_3, α_3) on the HF degeneration dynamics. In addition, from the stochastic simulations, we notice that the Mx compartment size still has a large variance in all three simulations, compared to other compartments. Since the Mx compartment size is highly dynamic, the periodic dynamic pattern shown in the deterministic simulation (8B) is not very clear in the stochastic simulation (8B′), though the apoptosis cell number still shows some hints of the periodicity despite that it is also not very noticeable due to the small cell number (8B′, black solid line)

We continue our bifurcation analysis on the apoptosis feedback strengths by making a simplifying assumption on the model and letting $p = p_2 = p_3$ The values of α_2 and α_3 are fixed as the 5.5 Gy calibrated values. For small values of s_3, increasing the bifurcation parameter p induces a decrease in both ORS_q and Mx stable steady state values, together with a slight increase in apoptosis steady state value (Fig. 9A). As the apoptosis feedback strength ($p = p_2 = p_3$) keeps increasing, a Hopf bifurcation is triggered and the system enters the periodic solution domain. On the other hand, when s_3 is larger, no bifurcation occurs as p varies, and increasing the apoptosis feedback strength p causes a decrease in ORS_q and Mx stable steady state values, together with an increases in the apoptosis steady state value. Also refer to example dynamic simulations in Fig. 8.

Finally, we point out that catagen is a transient phase that is typically much shorter than anagen or telogen. If the Mx cells' spontaneous apoptosis rate (s_3) increases fast at the anagen-to-catagen transition, it may push the system quickly from the anagen homeostatic state (small s_3) to the degenerating state (large s_3), completely bypassing the periodic behavior. This is illustrated by our simulation of the anagen-to-catagen transition dynamics in Fig. 10, where we set up a linear increase of s_3 from day 5 to day 10 (Fig. 10A). The resulting deterministic dynamics and a sample path from the stochastic simulation are shown in Fig. 10BC, respectively, from which we see that the increase in s_3 steadily induces the degeneration of the HF, and we hardly see any periodic dynamics. This may explain why periodicity is not observed in experiments. In addition, during catagen, more complicated morphological deformations occur in the HF, therefore at the late catagen stage, our cell differentiation population model might no longer be adequate.

5. Conclusions and discussions

In this paper, we developed a new ODE type of HF cell differentiation population model, and used it to investigate the underlying mechanisms of the IR induced HF regeneration and the catagen HF degeneration. The model for controlled mice includes four cell states—quiescent ORS, active ORS, Mx and apoptosis cells. While the last three types of cells together make up the dynamic part at the bottom of an anagen HF, the HF length can be estimated by the size of ORS – including both quiescent and active ORS – as ORS forms the outer concentric epithelial layer of the HF (Fig. 1B), and it connects the bulge stem cell niche near the top of the HF and the HF dynamic part at the bottom. We also extended this model by adding another state representing the radiated Mx cells, and used this extended model to study the IR induced HF regeneration dynamics. Model parameters were calibrated

from IR experimental data, subjected to either 2 Gy or 5.5 Gy IR. Data calibration results showed a good match between the model and the data, especially in the 2 Gy IR system, though in the 5.5 Gy IR system, the model showed a slower HF regeneration compared to the data. With the calibrated model, we performed both deterministic ODE simulations and the corresponding stochastic simulations. Both validate the regenerative dynamics induced by IR. We then applied stability, sensitivity and bifurcation analyses to the model, where it is revealed that during anagen, due to the extremely low spontaneous apoptosis rates in epithelial cells (s_2, s_3), the homeostatic anagen HF steady state is stable, and does not depend on the apoptosis feedback strength (p_2, α_2, p_3, α_3). This explains why an anagen HF is always able to return to its homeostatic state despite large scale degeneration caused by strong IR. Sensitivity analysis revealed a few factors that are important to the HF regenerative ability, including ORS cell proliferation, and that though the apoptosis feedback strength does not affect the HF regeneration in controlled mice, Mx cells' apoptosis feedback strength (p_3, α_3) may indeed affect the HF regeneration when subjected to IR. Further bifurcation analysis revealed that to push the HF from the anagen homeostasis to the irreversible degeneration in catagen, the system needs both Mx cells' spontaneous apoptosis rate (s_3) and the apoptosis feedback strength (p_2, p_3) to be strong. A transient periodic domain was revealed from the bifurcation analysis and the simulations, though in reality, a fast anagen-to-catagen transition may quickly push the system from the anagen steady state to the catagen steady state, without clearly showing the periodic dynamics—yet further experimental and modeling research would be needed to confirm this prediction.

Our model provides a mathematical explanation of the underlying mechanisms of an anagen HF, IR-induced regenerative dynamics and the catagen degenerative dynamics, and it provides potential guidance in future HF biology experimental research and radio-therapeutic study. There are several directions that can be further improved in the future. Currently in our model, there are two major simplifying assumptions: (1) while ORS is a continuum whose activation and quiescence is regulated by signaling gradients, in our model we assume them to be two sub-states as *active* and *quiescent* ORS, and (2) the HF length control in our system is currently modeled phenomenologically by Eq. (6), where in reality, this mechanism has not yet been identified in current HF biology. In the future, a PDE type of cell differentiation population model incorporating the spatial information in HF growth—or more specifically, the growth of the ORS, might well substitute our assumption of the *active* and *quiescent* ORS sub-states, and provide more accurate description and better insights of the HF regeneration dynamics. We also expect more biological evidence to emerge in the future, from which we can improve on the HF length control function in a more mechanistic way. We also point out that in our current parameter calibration, while the results show good match with the 2 Gy IR data, in the 5.5 Gy IR case, it seems that the experimental data shows a faster ORS-to-Mx flow right after the IR application as well as a faster HF regeneration when compared to our model. We suspect that this is partially due to our simple assumption of the HF length control mechanism (Eq. (6)). In addition, further modeling development on the signaling regulation might also be helpful. Currently in our model we include signal A - which may represent for example Tnf - that regulates HF epithelial cells' apoptosis, and signal B - which may represent Wnt and Shh - that regulates ORS cells' proliferation. However, Shh may also play a role in regulating Mx cell

proliferation, by either directly signaling to Mx or indirectly signaling to DP to perturb other signals affecting Mx cell proliferation. Furthermore, there are other well-known signaling pathways that cooperatively regulate HF growth, for example, Bmp, Tgf-β and Fgf. How these signals react to IR and thus regulate the HF regeneration needs to be explored from both experimental and modeling sides.

Finally, recent experimental research also reveal the HF degenerative/regenerative dynamics after chemotherapy (Yue et al., 2021; Haslam et al., 2021): when the HF is exposed to a low level of chemo-drug, the HF is able to stay in anagen despite a damaged hair fibre, referred to as the dystrophic anagen; on the other hand, when exposed to a high level of chemo-drug, the HF enters catagen and starts degeneration, followed by telogen until it enters the next anagen phase, referred to as the dystrophic catagen. While the low level chemo-drug induced dystrophic anagen shares some similarities with the 2 Gy IR-induced HF regeneration, the high level chemo-drug induced dystrophic catagen is very different from the 5.5 Gy IR-induced HF regeneration. What causes the difference between the chemo- vs. IR-induced HF degenerative/regenerative dynamics is an interesting question and needs further investigations on both experimental and modeling sides, and we suspect that though some similarities probably exist, chemotherapy and IR may trigger different signaling pathways that lead to the different regenerative dynamics. For example, it is reported that Shh may play a bigger role in the chemo-drug induced HF degenerative dynamics, comparing to in the IR-induced HF regenerative dynamics (Yue et al., 2021; Haslam et al., 2021; Huang et al., 2017). Considering that disrupting the Shh signal may inhibit Mx cell proliferation leading to HF degeneration, and that Mx is a major source of Shh signal, how such feedback affects the chemo- vs. IR-induced HF degeneration/regeneration should be studied in the future.

Acknowledgments

The authors thank Dr. Wen-Yen Huang and Dr. Sung-Jan Lin for providing their original data published in Huang et al. (2017) and their stimulating conversations. The authors acknowledge support from the National Science Foundation, USA Grant DMS-1951184 to Q.W..

Data availability

Data will be made available on request.

Appendix A. Derivation of the HF cell differentiation population model Eqs. (1)

The formulation of the HF model (Eqs. (1)) mostly follows the classic cell differentiation population model, which can be found in literature including (Lo et al., 2009; Lander et al., 2009; Doumic et al., 2011; Marciniak-Czochra et al., 2009). Below we briefly justify the formulation of Eqs. (1) together with the constraints Eqs. (2).

Consider Eq. (1b) for ORS_a. First, in the case that $f([\mathrm{ORS}_a](t)) > 0$, that is, there is an inflow from ORS_q to ORS_a, during a short time period $[t, t + \Delta t)$ the change in ORS_a cell number

consists of two parts: the part that comes from ORS_a transition (denoted by I_1), and the part that comes from ORS_a cells' proliferation/differentiation/apoptosis (denoted by I_2):

$$[ORS_a](t+\Delta t) - [ORS_a](t) \approx I_1 + I_2$$

It is easy to see that during the short time period $[t, t+\Delta t)$,

$$I_1 \approx f([ORS_a](t))\Delta t$$

ORS_a cell divisions happen at the frequency of ν_{ORS}. The classic cell differentiation population model assumes that on the population level, on average, all cells undergo divisions at the same frequency; or in plain words, all cells divide into two at the frequency ν_{ORS}. In addition, here we adopt the symmetric division assumption, that is, as a cell divides, it gives rise to two daughter cells of the same type. With the symmetric division, if the two daughter cells are of the same type of their dividing mother cell, we refer it to as proliferation; otherwise, if the two daughter cells are of a progeny type of their diving mother cell, then it is referred to as differentiation. In our follicle model, since we also consider the apoptosis cells as a transient cell type, we adopt the "differentiation" formulation for apoptosis cells, with the difference that instead of dividing into two, one ORS_a cell turns into one apoptosis cell. The dividing relations of ORS_a are summarized in Fig. A.11.

From these assumptions, that all ORS_a cells divide at the frequency ν_{ORS}, and each dividing cell either proliferates, differentiates, or undergoes apoptosis, we obtain the constraint Eq. (2a), that is, the portion of proliferating, differentiating and apoptosis ORS_a cells should sum up to 1. Therefore, the net change in ORS_a cell number due to cell division during $[t, t+\Delta t)$ is

$$I_2 \approx (2p^p_{ORS} - 1)[ORS_a](t)\Delta t$$

where -1 comes from that all ORS_a cell divide, and $2p^p_{ORS}$ comes from that p^p_{ORS} of the dividing ORS_a cells proliferate, that is, turn into 2 daughter ORS_a cells. Similarly, it can be derived that after the dividing, there will be $2p^d_{ORS}[ORS_a]$ newly differentiated Mx cells from ORS_a, and $p^a_{ORS}[ORS_a]$ apoptosis cells from ORS_a—again notice that unlike the proliferating and differentiating cells, we assume that one ORS_a cell turns into only one apoptosis cell. Therefore we obtain

$$\begin{aligned}[ORS_a](t+\Delta t) - [ORS_a](t) &\approx I_1 + I_2 \\ &= f([ORS_a](t))\Delta t + (2p^p_{ORS}(t) - 1)\nu_{ORS}[ORS_a](t)\Delta t\end{aligned}$$

which gives Eq. (1b):

$$\begin{aligned}\frac{d[ORS_a]}{dt} &= \lim_{\Delta t \to 0} \frac{[ORS_a](t+\Delta t) - [ORS_a](t)}{\Delta t} \\ &= f([ORS_a]) + (2p^p_{ORS} - 1)\nu_{ORS}[ORS_a]\end{aligned}$$

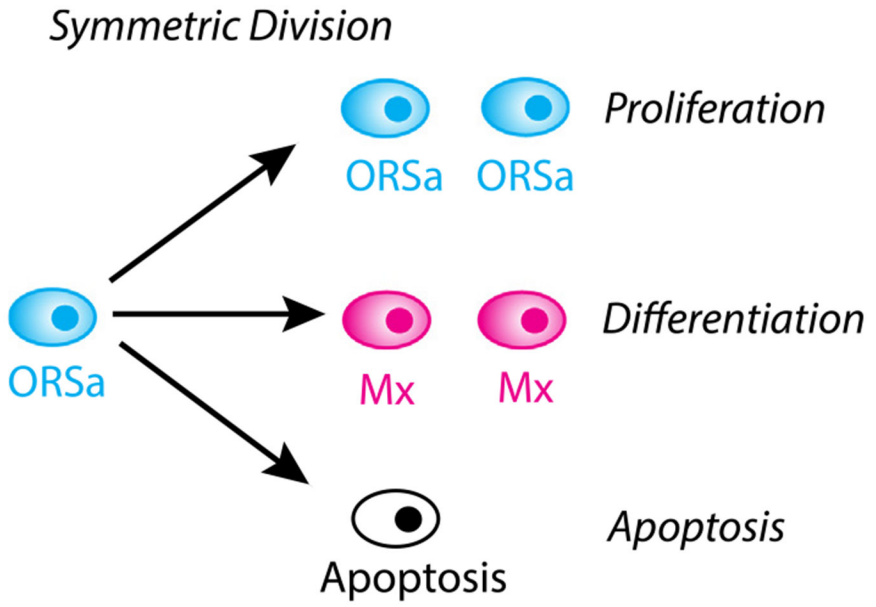

Fig. A.11.
An illustration diagram of the symmetric divisions of ORS_a cells in the HF model.

In the case that $f([ORS_a](t)) < 0$, that is, there is an outflow from ORS_a to ORS_q, we assume that $|\, f([ORS_a](t))\,| \sim O(1)$. In addition, since generally speaking, the ORS_a-to-ORS_q transition and ORS_a cell divisions happen at different frequencies, we may roughly consider that in a short time period $[t, t+\Delta t)$ the ORS_a-to-ORS_q transition and the ORS_a cell division happen successively. That is, if the transition happens in the interval $[t, t+\Delta t)$, then the ORS_a cells divide at $t+\Delta t$. Therefore, the ORS_a cell number right before the cell division is

$$\lim_{\tau \to (t+\Delta t)^-} [ORS_a](\tau) \approx [ORS_a](t) + f([ORS_a](t))\Delta t$$

then at $t+\Delta t$, ORS_a cell divisions will lead to a change in the ORS_a cell number as

$$(2p^p_{ORS}(t) - 1)([ORS_a](t) + f([ORS_a](t))\Delta t)$$

Notice that the constraint Eq. (2a) still holds; we are only considering the dividing ORS_a cells since the ORS_a-to-ORS_q transition mostly happens at a different frequency, and we have included the transition term inside the current ORS_a cell number. Therefore, we get the estimate

$$[ORS_a](t+\Delta t) - [ORS_a](t) \approx \\ [f([ORS_a](t)) + (2p^p_{ORS}(t) - 1)v_{ORS}([ORS_a](t) + f([ORS_a](t))\Delta t)]\Delta t$$

Under the assumption of $|\, f([ORS_a](t))\,| \sim O(1)$, we have

$$\frac{[\mathrm{ORS}_a](t+\Delta t)-[\mathrm{ORS}_a](t)}{\Delta t} \approx f([\mathrm{ORS}_a](t)) + (2p^p_{\mathrm{ORS}}-1)\nu_{\mathrm{ORS}}[\mathrm{ORS}_a] + o(\Delta t)$$

Let $\Delta t \to 0$, again we get Eq. (1b):

$$\frac{d[\mathrm{ORS}_a]}{dt} = f([\mathrm{ORS}_a]) + (2p^p_{\mathrm{ORS}}-1)\nu_{\mathrm{ORS}}[\mathrm{ORS}_a]$$

We point out that though we could not rigorously prove it, the assumption $|f([\mathrm{ORS}_a](t))| \sim O(1)$ mostly holds true when $f([\mathrm{ORS}_a](t)) < 0$ in our system. Notice that $f([\mathrm{ORS}_a](t)) < 0$, or equivalently, the ORS_a-to-ORS_q transition, only happens when the ORS_a cell number ($[\mathrm{ORS}_a]$) exceeds the equilibrium size (C_{ORS}). To break the constraint $|f([\mathrm{ORS}_a](t))| \sim O(1)$, it needs a very large ORS_a cell number, which is rarely the case in either a controlled system or a radiated system. This can also be seen from our simulation results (for example, Fig. 4).

We have shown that in either ORS_a inflow or outflow case, Eq. (1b) holds, though in the outflow case, some condition applies. We also point out that if we consider the size of the entire ORS as $[\mathrm{ORS}_q] + [\mathrm{ORS}_a]$, the only change in the cell number comes from cell proliferation, differentiation and apoptosis, which can be obtained by adding up Eqs. (1a) and (1b):

$$\frac{d[\mathrm{ORS}_q]}{dt} + \frac{d[\mathrm{ORS}_a]}{dt} = (2p^p_{\mathrm{ORS}}-1)\nu_{\mathrm{ORS}}[\mathrm{ORS}_a]$$

Analogously, Eqs. (1c) (1d) for Mx and apoptosis cells can be derived in a similar way. In (1c), $(2p^p_{\mathrm{Mx}}-1)\,\nu_{\mathrm{Mx}}[\mathrm{Mx}]$ comes from the dividing of Mx cells, and $2p^d_{\mathrm{ORS}}\,\nu_{\mathrm{ORS}_a}[\mathrm{ORS}_a]$ comes from the differentiating ORS_a cells, with the constraint Eq. (2b) for dividing Mx cells. In (1d), $p^a_{\mathrm{ORS}}\,\nu_{\mathrm{ORS}_a}[\mathrm{ORS}_a]$ comes from the apoptosis of ORS_a cells, $p^a_{\mathrm{Mx}}\nu_{\mathrm{Mx}}[\mathrm{Mx}]$ comes from the apoptosis of Mx cells, and since apoptosis cells die, or say, leave the system at the rate d, it leads to the $-d[\mathrm{Apop}]$ term.

Appendix B. Further data-model comparison

In this part, we show our model results when simulating Mx proliferation and the ORS-to-Mx differentiation dynamics and compare to the experimental data. We did not use this data in our parameter calibration, since, as we will explain below, the simulated terms are only approximations to what is measured in experiments.

We first compare the proliferating Mx cells (defined as $\nu_{\mathrm{Mx}}p^p_{\mathrm{Mx}}[\mathrm{Mx}]$) to the BrdUrd+ Mx cell data (Fig. B.12AA′). In the experimental 2 Gy IR case, BrdUrd+ Mx data indicates that Mx cells return to proliferation soon after radiation, while in the 5.5 Gy IR case, two proliferation restoration attempts can be observed, both of which stay at low levels. The increase in proliferation after day 3 is what we characterize as the second regeneration

attempt. When observing the simulation results, proliferation in the 2 Gy case exhibits an immediate sharp increase which quickly appears to settle at a similar level as the experimental data. On the other hand, proliferation in the 5.5 Gy simulations fail to capture the two regeneration attempts (Fig. 4C), although when looking close, we do see a small sharp increase and decrease in proliferation very early, followed by another, much more slow increase. Additional mechanisms might contribute to this second regeneration attempt, which need to be investigated.

Next, we simulated the K5+ Mx cell lineage by tracking the Mx cells that were derived either from Mx ([Mx−]) or ORS ([Mx+]) after IR is applied, which indicate the ORS-to-Mx flow in the model. We compare the results with the K5+ Mx cell data. Both the 2 Gy and 5.5 Gy IR experimental observations show a quick increase in K5+ Mx cells at early stage (Fig. B.12B′ blue squares), indicating a fast upward migration of Mx cells after radiation, which is possibly driven by a quick ORS-to-Mx flow. Computationally, in the 2 Gy IR simulation, during the early stage, ORS cells steadily flow into Mx (Fig. B.12B red solid line); while in the 5.5 Gy IR simulation, a slow early ORS-to-Mx flow is followed by a sudden increase in the flow speed (Fig. B.12B′ red solid line), occurring significantly later than in the experimental observations. This may indicate that additional mechanisms are needed to drive the early ORS-to-Mx flow when subject to strong IR. We point out that observing K5+ Mx cells is not exactly the same as a lineage tracing experiment. This can be easily understood from the decrease in the K5+ Mx cell number soon after the early sudden increase (Fig. B.12BB′, blue boxes), which would not be seen in a lineage tracing experiment. This results in the long term behavior of K5+ Mx cell data being essentially different from our simulations, though they share some similarity at the early stage. Finally, in both 2 Gy and 5.5 Gy simulations, there is a quick and significant increase in Mx cells derived from radiated Mx cells returning normal and their proliferation (Fig. B.12B red dashed lines).

Appendix C. Posterior distributions of the parameters

In this part, we produce the posterior distributions of the model parameters using the ABC rejection sampler method (Warne et al., 2019). We consider the 2 Gy and 5.5 Gy IR simulations separately. Prior distributions are uniformly generated in intervals centered at each calibrated parameter value from the model, ranged from 0.5- to 1.5-fold. For each generated prior sample parameter set (denoted as $\boldsymbol{\theta}$, where depending if it is the marginal or pairwise distributions, one or two parameter values may be different from the calibrated parameter values), we generate a sample path from the stochastic model (Section 2.5), and compare the simulated data with the experiment data for apoptosis cell number, bulb cell number and HF length, respectively.

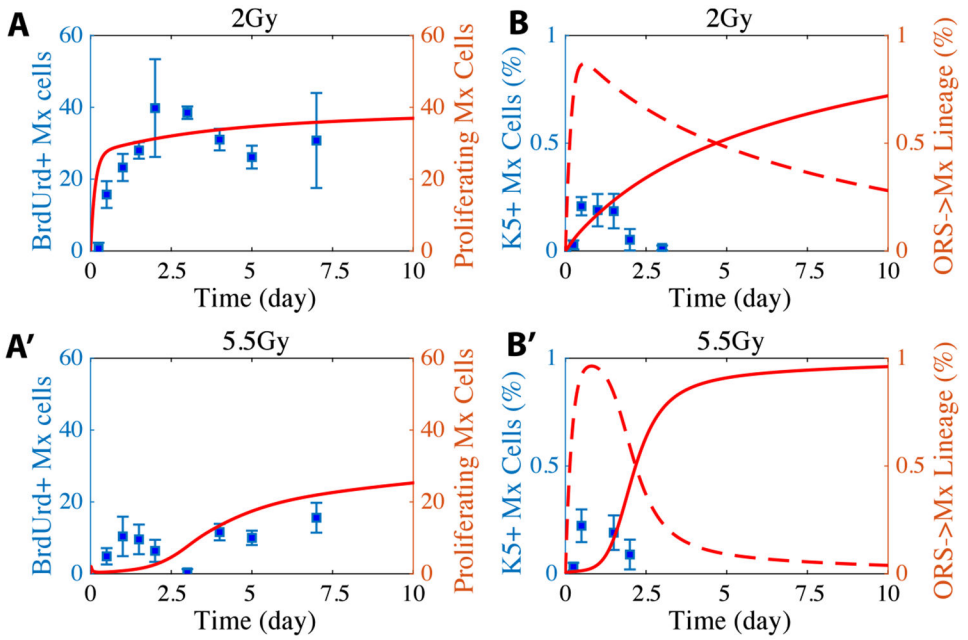

Fig. B.12.

Model-data comparison of the IR induced HF regeneration. Red lines show simulation results with the red *y*-axis on the right, blue boxes show experimental data with the blue *y*-axis on the left. **AB** show the simulations/experimental observations with 2 Gy IR, and **A′B′** show simulations/experimental observations with 5.5 Gy IR. **AA′** compare the simulated proliferating Mx cells and the BrdUrd+ Mx cells from experimental observations. **BB′** show the K5+ Mx cells and simulated ORS-to-Mx flow, with red solid lines showing the percentage of post-IR Mx cells that are derived from ORS, and red dashed lines showing the percentage of post-IR Mx cells that are derived from Mx cells.

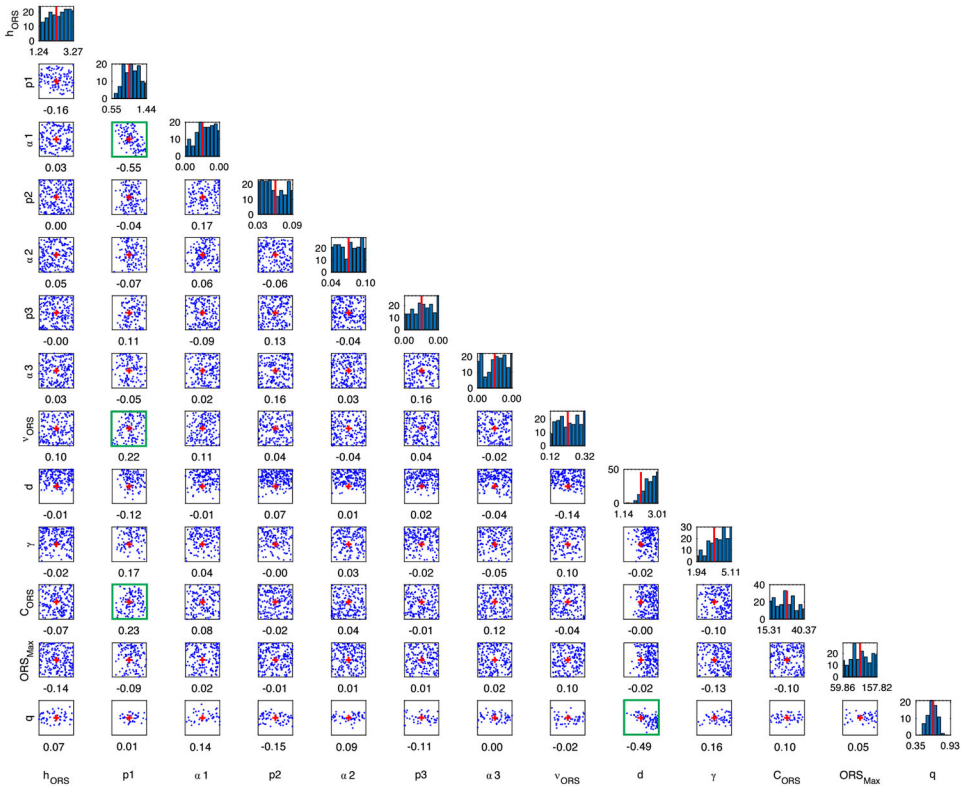

Fig. C.13.

Posterior distributions of the parameters for 2 Gy IR. The diagonal/off-diagonal plots show the marginal/pairwise posterior distributions of the parameters. Prior distributions are uniformly generated in intervals centered at each parameter value from the model, ranged from 0.5- to 1.5-fold, and the left and right end values of each parameter can be found in the *x*-axis of the diagonal plots. Red lines in the marginal plots and red + in the pairwise plots show the parameter values used in the model. The correlation of a pair of parameters are given by the number under the corresponding pairwise plots. Pairwise plots with the green borders indicate the two parameters showing relatively larger correlations.

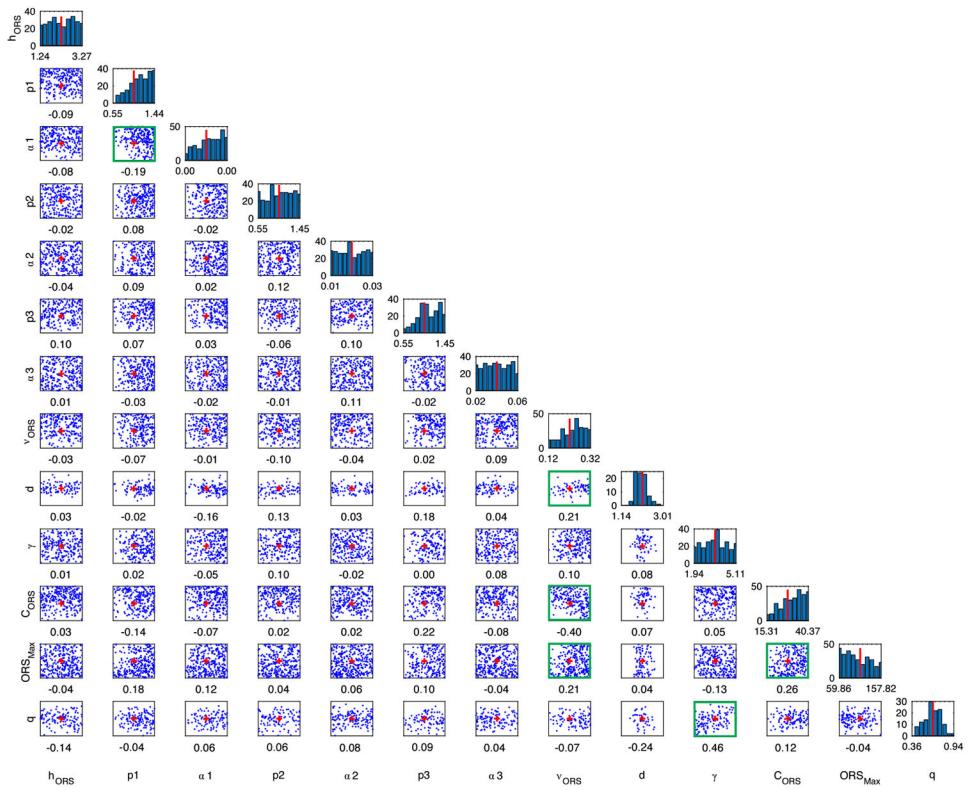

Fig. C.14.

Posterior distributions of the parameters for 5.5 Gy IR. The diagonal/off-diagonal plots show the marginal/pairwise posterior distributions of the parameters. Prior distributions are uniformly generated in intervals centered at each parameter value from the model, ranged from 0.5- to 1.5-fold, and the left and right end values of each parameter can be found in the *x*-axis of the diagonal plots. Red lines in the marginal plots and red + in the pairwise plots show the parameter values used in the model. The correlation of a pair of parameters are given by the number under the corresponding pairwise plots. Pairwise plots with the green borders indicate the two parameters showing relatively larger correlations.

Table E.1

Cellular processes in the stochastic model. For simplicity, we denote the cell number of each HF compartment as ORS_q - x, ORS_a - y, Mx – z, Apop - w, Mx^{IR} - z^*.

Reaction	Reaction rate	Cell number change				
		x	y	z	w	z^*
$\mathrm{ORS}_q \rightarrow \mathrm{ORS}_a$	$\max\{0, h_{\mathrm{ORS}}(C_{\mathrm{ORS}} - y)\}$	−1	1	0	0	0
$\mathrm{ORS}_a \rightarrow \mathrm{ORS}_q$	$\max\{0, h_{\mathrm{ORS}}(y - C_{\mathrm{ORS}})\}$	1	−1	0	0	0
$\mathrm{ORS}_a \rightarrow 2\,\mathrm{ORS}_a$	$\nu_{\mathrm{ORS}}\, p^p_{\mathrm{ORS}}(x, z, w)y$	0	1	0	0	0
$\mathrm{ORS}_a \rightarrow \mathrm{Apop}$	$\nu_{\mathrm{ORS}}\, p^a_{\mathrm{ORS}}(w)y$	0	−1	0	1	0
$\mathrm{ORS}_a \rightarrow 2\,\mathrm{Mx}$	$\nu_{\mathrm{ORS}}(1 - p^a_{\mathrm{ORS}}(w) - p^p_{\mathrm{ORS}}(x, z, w))y$	0	−1	2	0	0

Reaction	Reaction rate	Cell number change				
		x	y	z	w	z^*
$\mathrm{Mx} \rightarrow 2\,\mathrm{M}$	$\nu_{\mathrm{Mx}} r(1-p^a_{\mathrm{Mx}}(w))z$	0	0	1	0	0
$\mathrm{Mx} \rightarrow \phi$	$\nu_{\mathrm{Mx}}(1-r)(1-p^a_{\mathrm{Mx}}(w))z$	0	0	−1	0	0
Mx→Apop	$\nu_{\mathrm{Mx}}\, p^a_{\mathrm{Mx}}(w)z$	0	0	0	−1	0
$\mathrm{Apop} \rightarrow \phi$	dw	0	0	−1	0	0
$\mathrm{Mx}^{IR} \rightarrow \mathrm{Mx}$	$\gamma q z^*$	0	0	1	0	−1
$\mathrm{Mx}^{IR} \rightarrow \mathrm{Apop}$	$\gamma(1-q)z^*$	0	0	0	1	−1

The data-simulation discrepancy metric is defined as

$$\rho(Y,S)=\left[\sum_{t_i}(Y(t_i)-S(t_i))^2\right]^{1/2}$$

where t_i is the data time-points, with $t_i \in \{0h, 6h, 12h, 1d, 1.5d, 2d, 3d, 4d, 5d, 7d\}$, h stands for hour and d stands for day; Y is the average of the experimental data and S is the simulated data, and they can be the apoptosis cell number (Y_a, S_a), bulb cell number (Y_b, S_b) or HF length (Y_l, S_l). We set thresholds ε_a, ε_b, ε_l for apoptosis cell number, bulb cell number and HF length, respectively. If a sample path generated from a parameter value set $\boldsymbol{\theta}$ satisfies all of the following conditions

$$\rho(Y_a,S_a)<\varepsilon_a,\quad \rho(Y_b,S_b)<\varepsilon_b,\quad \rho(Y_l,S_l)<\varepsilon_l$$

we accept $\boldsymbol{\theta}$ in the posterior distribution, otherwise we do not.

Table E.2

Parameter values of the HF model calibrated from the IR experimental data.

Parameters	Values
s_2	0
s_3	0
ν_{Mx}	ln 2
E_{Mx}	128
h_{ORS}	2.25
ν_{ORS}	0.22
d	2.08
C_{ORS}	27.84
$\mathrm{ORS}_{\mathrm{max}}$	108.84
γ	3.53

Parameters	Values	
p_1	0.99	
p_2	5.94×10^{-2} (2 Gy)	0.99 (5.5 Gy)
p_3	1.53×10^{-4} (2 Gy)	0.99 (5.5 Gy)
α_1	6.16×10^{-5}	
α_2	7.13×10^{-2} (2 Gy)	2.27×10^{-2} (5.5 Gy)
α_3	3.25×10^{-3} (2 Gy)	4.26×10^{-2} (5.5 Gy)
q	0.64 (2 Gy)	0.65 (5.5 Gy)

Fig. C.13 shows the marginal and pairwise posterior distributions of 2 Gy IR with $\varepsilon_a = 6$, $\varepsilon_b = 60$, $\varepsilon_l = 0.3$, and Fig. C.14 shows the marginal and pairwise posterior distributions of 2 Gy IR with $\varepsilon_a = 8$, $\varepsilon_b = 60$, $\varepsilon_l = 0.8$. The correlation of two variables are given by the number under the corresponding pairwise plot. In 2 Gy IR (Fig. C.13), p_1 and α_1 show a strong negative correlation (−0.55). Notice that to keep a controlled HF in the equilibrium state, p_1 and α_1 have to satisfy the constraint Eq. (11a), therefore it is not surprising that p_1 and α_1 are strongly negatively correlated. Besides p_1 and α_1, d and q also show a strong negative correlation (−0.49), and p_1 shows slight positive correlations with v_{ORS} (0.22) and C_{ORS} (0.23). In 5.5 Gy IR (Fig. C.14), p_1 and α_1 shows a slight negative correlation (−0.19) but not as strong as in 2 Gy IR. q and γ show a strong positive correlation (0.46). $v_{\text{ORS}} \sim d$ (0.21), $v_{\text{ORS}} \sim \text{ORS}_{\text{max}}$ (0.21), $\text{ORS}_{\text{max}} \sim C_{\text{ORS}}$ (0.26) show slight positive correlation, and $C_{\text{ORS}} \sim v_{\text{ORS}}$ (−0.4) show a slight negative correlation.

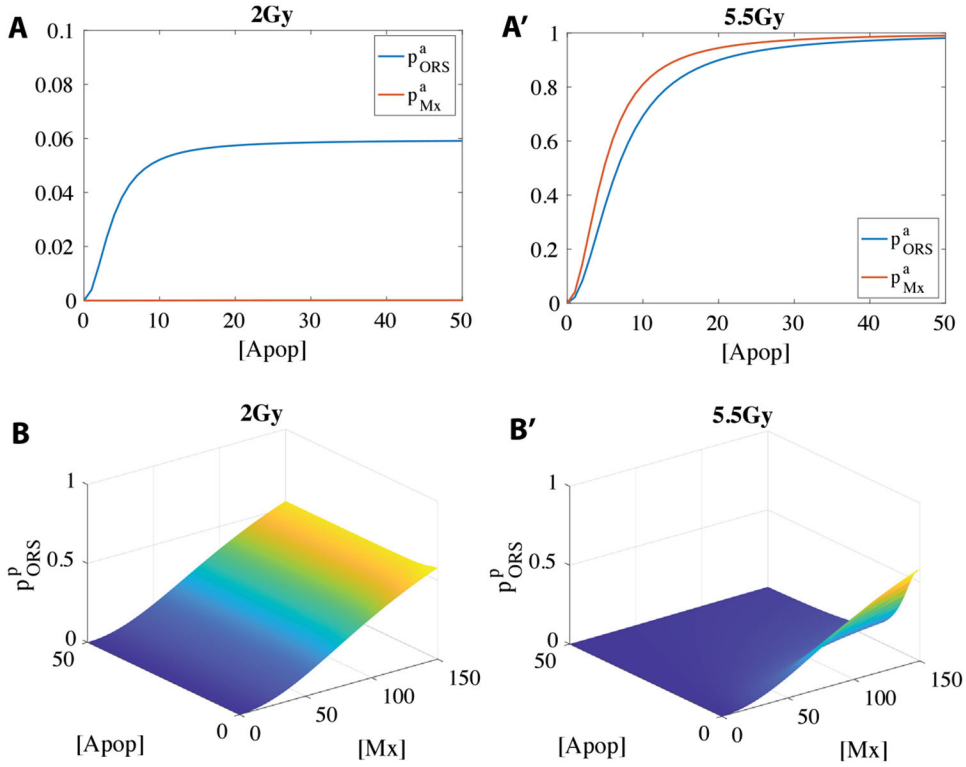

Fig. E.15.

Figures of p^{a}_{ORS} (Eq. (4a)), p^{a}_{Mx} (Eq. (4b)), and p^{p}_{ORS} (Eq. (5)). Parameters values are taken from the 2 Gy (**AB**) and 5.5 Gy (**A′B′**) simulations, respectively (Table E.2). In the plots of p^{p}_{ORS} (**BB′**), we take $[\mathrm{ORS}_q] = E_q$ so that p^{p}_{ORS} depends on [Apop] and [Mx].

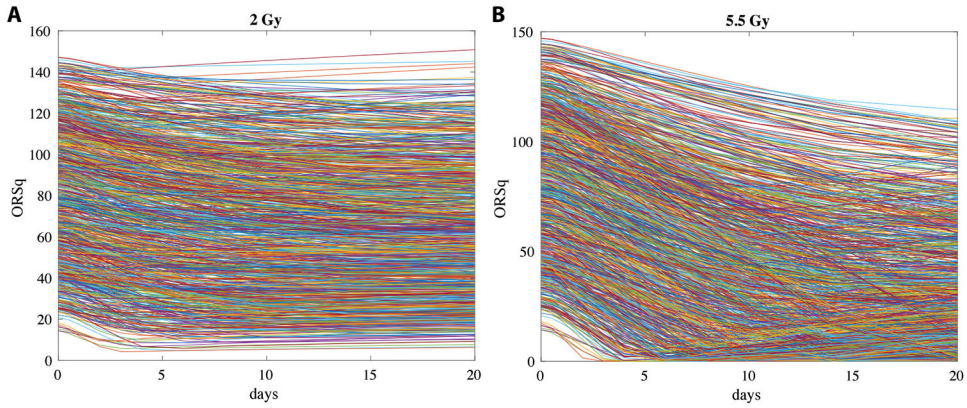

Fig. E.16.

Trajectories of ORS_q with parameters generated by LHS in the PRCC performance.

Table E.3

Parameter values of p_2, α_2, p_3, α_3 in the bifurcation diagrams from Fig. 7. IS stands for "intermediate system".

	2 Gy IR	IS 1	IS 2	IS 3	IS 4	5.5 Gy IR
p_2	5.94×10^{-2}	0.1	0.4	0.7	0.8	0.99
α_2	7.13×10^{-2}	0.05	0.03	0.02	0.021	2.27×10^{-2}
p_3	1.53×10^{-4}	0.1	0.4	0.7	0.8	0.99
α_3	3.25×10^{-3}	0.01	0.02	0.03	0.04	4.26×10^{-2}

Appendix D. Linear stability analysis of the anagen homeostatic steady state

We perform a linear stability analysis to the system Eq. (1) at the steady state (E_q, C_{ORS}, E_{Mx}, 0). For simplicity, we denote [ORS_q], [ORS_a], [Mx], [Apop] as x_1, x_2, x_3, x_4, respectively. During anagen, with the assumption $s_2 = s_3 = 0$, the Jacobian at this steady state is

$$J = \begin{pmatrix} 0 & h_{\mathrm{ORS}} & 0 & 0 \\ E & A & B & 0 \\ F & C & D & 0 \\ 0 & 0 & 0 & -d \end{pmatrix}$$

where

$$\begin{aligned} E &= -\frac{\nu_{\mathrm{ORS}} C_{\mathrm{ORS}}}{E_q} \\ A &= -h_{\mathrm{ORS}} \\ B &= 2\nu_{\mathrm{ORS}} C_{\mathrm{ORS}} p_1 \frac{2\alpha_1 E_{\mathrm{Mx}}}{(1+\alpha_1 E_{\mathrm{Mx}}^2)^2} = \frac{2\nu_{\mathrm{ORS}} C_{\mathrm{ORS}}}{E_{\mathrm{Mx}}(1+\alpha_1 E_{\mathrm{Mx}}^2)} \\ C &= \nu_{\mathrm{ORS}} \\ D &= -\frac{2\nu_{\mathrm{ORS}} C_{\mathrm{ORS}}}{E_{\mathrm{Mx}}(1+\alpha_1 E_{\mathrm{Mx}}^2)} + \nu_{\mathrm{Mx}}(2r-1) \end{aligned}$$

With the calibrated parameter values from the IR experiment data, the above Jacobian yields four eigenvalues:

$$\lambda_1 = -d = -2.0755,\ \lambda_2 = -2.1785,\ \lambda_3 = -0.0258,\ \lambda_4 = -0.1440$$

all of which are negative, indicating that the homeostatic steady state of an anagen HF is stable. Moreover, notice that the parameters participating in the apoptotic events (α_2, p_2, α_3, p_3) do not show up in the Jacobian, indicating that this steady state remains stable under normal conditions (no IR), and is independent of these parameter values.

Appendix E. Supplementary tables and figures

In this part we present the reaction details in the stochastic model (Table E.1), the parameter values calibrated from the IR experimental data (Table E.2), the parameters used in the bifurcation plots (Table E.3), the plots of p^{a}_{ORS} (Eq. (4a)), p^{a}_{Mx} (Eq. (4b)), and p^{p}_{ORS} (Eq. (5)) (Fig. E.15), and the trajectories generated by LHS in the PRCC performance (Fig. E.16).

References

Al-Nuaimi Y, Goodfellow M, Paus R, Baier G, 2012. A prototypic mathematical model of the human hair cycle. J. Theoret. Biol 310, 143–159. [PubMed: 22677396]

Blessing M, Nanney L, King L, Jones C, Hogan B, 1993. Transgenic mice as a model to study the role of TGF-beta-related molecules in hair follicles. Genes Dev. 7 (2), 204–215. 10.1101/gad.7.2.204. [PubMed: 8436293]

Botchkarev VA, 2003. Bone morphogenetic proteins and their antagonists in skin and hair follicle biology. J. Invest. Dermatol. 120 (1), 36–47. 10.1046/j.1523-1747.2003.12002.x. [PubMed: 12535196]

Botchkarev VA, Botchkareva NV, Roth W, Nakamura M, Chen L-H, Herzog W, Lindner G, McMahon JA, Peters C, Lauster R, et al. , 1999. Noggin is a mesenchymally derived stimulator of hair-follicle induction. Nature Cell Biol. 1 (3), 158–164. 10.1038/11078. [PubMed: 10559902]

Botchkarev VA, Kishimoto J, 2003. Molecular control of epithelial–mesenchymal interactions during hair follicle cycling. In: Journal of Investigative Dermatology Symposium Proceedings, Vol. 8. Elsevier, pp. 46–55. 10.1046/j.1523-1747.2003.12171.x. [PubMed: 12894994]

Botchkareva NV, Ahluwalia G, Shander D, 2006. Apoptosis in the hair follicle. J. Invest. Dermatol 126 (2), 258–264. 10.1038/sj.jid.5700007. [PubMed: 16418734]

Celso CL, Prowse DM, Watt FM, 2004. Transient activation of β-catenin signalling in adult mouse epidermis is sufficient to induce new hair follicles but continuous activation is required to maintain hair follicle tumours.

Dinh K, Wang Q, 2022. A probabilistic Boolean model on hair follicle cell fate regulation by TGF-β. Biophys. J 121 (13), 2638–2652. [PubMed: 35714600]

Doumic M, Marciniak-Czochra A, Perthame B, Zubelli JP, 2011. A structured population model of cell differentiation. SIAM J. Appl. Math 71 (6), 1918–1940. 10.1137/100816584.

Driskell RR, Clavel C, Rendl M, Watt FM, 2011. Hair follicle dermal papilla cells at a glance. J. Cell Sci 124 (8), 1179–1182. 10.1242/jcs.082446. [PubMed: 21444748]

Eroglu M, Derry W, 2016. Your neighbours matter–non-autonomous control of apoptosis in development and disease. Cell Death Differ. 23 (7), 1110–1118. 10.1038/cdd.2016.41. [PubMed: 27177021]

Gillespie DT, et al. , 2007. Stochastic simulation of chemical kinetics. Annu. Rev. Phys. Chem 58 (1), 35–55. [PubMed: 17037977]

Haake AR, Polakowska RR, 1993. Cell death by apoptosis in epidermal biology. J. Invest. Dermatol 101 (2), 107–112. 10.1111/1523-1747.ep12363594. [PubMed: 8345210]

Halloy J, Bernard BA, Loussouarn G, Goldbeter A, 2000. Modeling the dynamics of human hair cycles by a follicular automaton. Proc. Natl. Acad. Sci 97 (15), 8328–8333. [PubMed: 10899998]

Haslam IS, Zhou G, Xie G, Teng X, Ao X, Yan Z, Smart E, Rutkowski D, Wierzbicka J, Zhou Y, et al. , 2021. Inhibition of Shh signaling through MAPK activation controls chemotherapy-induced alopecia. J. Invest. Dermatol 141 (2), 334–344. [PubMed: 32682910]

Heitman N, Sennett R, Mok K-W, Saxena N, Srivastava D, Martino P, Grisanti L, Wang Z, Ma'ayan A, Rompolas P, et al. , 2020. Dermal sheath contraction powers stem cell niche relocation during hair cycle regression. Science 367 (6474), 161–166. [PubMed: 31857493]

Hsu Y-C, Fuchs E, 2012. A family business: stem cell progeny join the niche to regulate homeostasis. Nature Rev. Mol. Cell Biol 13 (2), 103–114. 10.1038/nrm3272.

Hsu Y-C, Li L, Fuchs E, 2014. Transit-amplifying cells orchestrate stem cell activity and tissue regeneration. Cell 157 (4), 935–949. 10.1016/j.cell.2014.02.057. [PubMed: 24813615]

Hsu Y-C, Pasolli HA, Fuchs E, 2011. Dynamics between stem cells, niche, and progeny in the hair follicle. Cell 144 (1), 92–105. 10.1016/j.cell.2010.11.049. [PubMed: 21215372]

Huang W-Y, Lai S-F, Chiu H-Y, Chang M, Plikus MV, Chan C-C, Chen Y-T, Tsao P-N, Yang T-L, Lee H-S, Chi P, Lin S-J, 2017. Mobilizing transit-amplifying cell-derived ectopic progenitors prevents hair loss from chemotherapy or radiation therapy. Cancer Res. 77 (22), 6083–6096. 10.1158/0008-5472. [PubMed: 28939680]

Huang W-Y, Lin ET-Y, Hsu Y-C, Lin S-J, 2019. Anagen hair follicle repair: timely regenerative attempts from plastic extra-bulge epithelial cells. Exp. Dermatol 28 (4), 406–412. [PubMed: 30664259]

Huelsken J, Vogel R, Erdmann B, Cotsarelis G, Birchmeier W, 2001. β-Catenin controls hair follicle morphogenesis and stem cell differentiation in the skin. Cell 105 (4), 533–545. [PubMed: 11371349]

Kligman AM, 1959. The human hair cycle. J. Invest. Dermatol 33 (6), 307–316. [PubMed: 14409844]

Kobielak K, Pasolli HA, Alonso L, Polak L, Fuchs E, 2003. Defining BMP functions in the hair follicle by conditional ablation of BMP receptor IA. J. Cell Biol 163 (3), 609–623. 10.1083/jcb.200309042. [PubMed: 14610062]

Kulessa H, Turk G, Hogan BL, 2000. Inhibition of bmp signaling affects growth and differentiation in the anagen hair follicle. EMBO J. 19 (24), 6664–6674. 10.1093/emboj/19.24.6664. [PubMed: 11118201]

Lander AD, Gokoffski KK, Wan FY, Nie Q, Calof AL, 2009. Cell lineages and the logic of proliferative control. PLoS Biol. 7 (1), e1000015. 10.1371/journal.pbio.1000015. [PubMed: 19166268]

Lindner G, Botchkarev VA, Botchkareva NV, Ling G, Van Der Veen C, Paus R, 1997. Analysis of apoptosis during hair follicle regression (catagen). Am. J. Pathol 151 (6), 1601. [PubMed: 9403711]

Lo W-C, Chou C-S, Gokoffski KK, Wan FY-M, Lander AD, Calof AL, Nie Q, 2009. Feedback regulation in multistage cell lineages. Math. Biosci. Eng.: MBE 6 (1), 59. 10.3934/mbe.2009.6.59. [PubMed: 19292508]

Malkinson FD, Keane JT, 1978. Hair matrix cell kinetics: a selective review. Int. J. Dermatol 17 (7), 536–551. 10.1111/j.1365-4362.1978.tb05997.x. [PubMed: 99375]

Marciniak-Czochra A, Stiehl T, Ho AD, Jäger W, Wagner W, 2009. Modeling of asymmetric cell division in hematopoietic stem cells—regulation of self-renewal is essential for efficient repopulation. Stem Cells Dev. 18 (3), 377–386. 10.1089/scd.2008.0143. [PubMed: 18752377]

Marino S, Hogue IB, Ray CJ, Kirschner DE, 2008. A methodology for performing global uncertainty and sensitivity analysis in systems biology. J. Theoret. Biol 254 (1), 178–196. [PubMed: 18572196]

Martino PA, Heitman N, Rendl M, 2021. The dermal sheath: An emerging component of the hair follicle stem cell niche. Exp. Dermatol 30 (4), 512–521. [PubMed: 33006790]

Matsuo K, Mori O, Hashimoto T, 1998. Apoptosis in murine hair follicles during catagen regression. Arch. Dermatol. Res 290 (3), 133–136. 10.1007/s004030050278. [PubMed: 9558488]

Millar SE, 2002. Molecular mechanisms regulating hair follicle development. J. Invest. Dermatol 118 (2), 216–225. 10.1046/j.0022-202x.2001.01670.x. [PubMed: 11841536]

Müller-Röver S, Rossiter H, Lindner G, Peters EM, Kupper TS, Paus R, 1999. Hair follicle apoptosis and Bcl-2. In: Journal of Investigative Dermatology Symposium Proceedings, Vol. 4. Elsevier, pp. 272–277. 10.1038/sj.jidsp.5640228. [PubMed: 10674380]

Müller-Röver S, Rossiter H, Paus R, Handjiski B, Peters EM, Murphy J-E, Mecklenburg L, Kupper TS, 2000. Overexpression of Bcl-2 protects from ultraviolet B-induced apoptosis but promotes hair follicle regression and chemotherapy-induced alopecia. Am. J. Pathol 156 (4), 1395–1405. [PubMed: 10751363]

Murray PJ, Maini PK, Plikus MV, Chuong C-M, Baker RE, 2012. Modelling hair follicle growth dynamics as an excitable medium. PLoS Comput. Biol 8 (12), e1002804. [PubMed: 23284275]

Painter K, Hunt G, Wells K, Johansson J, Headon D, 2012. Towards an integrated experimental–theoretical approach for assessing the mechanistic basis of hair and feather morphogenesis. Interface Focus 2 (4), 433–450. [PubMed: 23919127]

Painter KJ, Ptashnyk M, Headon DJ, 2021. Systems for intricate patterning of the vertebrate anatomy. Phil. Trans. R. Soc. A 379 (2213), 20200270. [PubMed: 34743605]

Parakkal PF, 1970. Morphogenesis of the hair follicle during catagen. Z. Zellforsch. Mikrosk. Anat 107 (2), 174–186. [PubMed: 5447672]

Paus R, Foitzik K, 2004. In search of the “hair cycle clock”: a guided tour. Differentiation 72 (9–10), 489–511. 10.1111/j.1432-0436.2004.07209004.x. [PubMed: 15617561]

Paus R, Rosenbach T, Haas N, Czarnetzki BM, 1993. Patterns of cell death: the significance of apoptosis for dermatology. Exp. Dermatol 2 (1), 3–10. 10.1111/j.1600-0625.1993.tb00192.x. [PubMed: 8156168]

Pérez-Garijo A, Fuchs Y, Steller H, 2013. Apoptotic cells can induce non-autonomous apoptosis through the TNF pathway. Elife 2, e01004. 10.7554/eLife.01004.001. [PubMed: 24066226]

Plikus MV, Baker RE, Chen C-C, Fare C, de la Cruz D, Andl T, Maini PK, Millar SE, Widelitz R, Chuong C-M, 2011. Self-organizing and stochastic behaviors during the regeneration of hair stem cells. Science 332 (6029), 586–589. [PubMed: 21527712]

Polakowska RR, Piacentini M, Bartlett R, Goldsmith LA, Haake AR, 1994. Apoptosis in human skin development: morphogenesis, periderm, and stem cells. Dev. Dyn 199 (3), 176–188. 10.1002/aja.1001990303. [PubMed: 7517223]

Rendl M, Polak L, Fuchs E, 2008. BMP signaling in dermal papilla cells is required for their hair follicle-inductive properties. Genes Dev. 22 (4), 543–557. 10.1101/gad.1614408. [PubMed: 18281466]

Rezza A, Wang Z, Sennett R, Qiao W, Wang D, Heitman N, Mok KW, Clavel C, Yi R, Zandstra P, et al. , 2016. Signaling networks among stem cell precursors, transit-amplifying progenitors, and their niche in developing hair follicles. Cell Rep. 14 (12), 3001–3018. 10.1016/j.celrep.2016.02.078. [PubMed: 27009580]

Rückert R, Lindner G, Bulfone-Paus S, Paus R, 2000. High-dose proinflammatory cytokines induce apoptosis of hair bulb keratinocytes in vivo. Br. J. Dermatol 143 (5), 1036–1039. [PubMed: 11069516]

Sato N, Leopold PL, Crystal RG, et al. , 1999. Induction of the hair growth phase in postnatal mice by localized transient expression of sonic hedgehog. J. Clin. Invest 104 (7), 855–864. [PubMed: 10510326]

Sennett R, Rendl M, 2012. Mesenchymal–epithelial interactions during hair follicle morphogenesis and cycling. In: Seminars in Cell & Developmental Biology, Vol. 23. Elsevier, pp. 917–927. 10.1016/j.semcdb.2012.08.011. [PubMed: 22960356]

Soma T, Ogo M, Suzuki J, Takahashi T, Hibino T, 1998. Analysis of apoptotic cell death in human hair follicles in vivo andin vitro. J. Invest. Dermatol 111 (6), 948–954. 10.1046/j.1523-1747.1998.00408.x. [PubMed: 9856801]

Stenn K, 1998. Growth of the hair follicle: a cycling and regenerating biological system. Mol. Basis Epithel. Append. Morphog.

Stenn K, Lawrence L, Veis D, Korsmeyer S, Seiberg M, 1994. Expression of the bcl-2 protooncogene in the cycling adult mouse hair follicle. J. Invest. Dermatol 103 (1), 107–111. [PubMed: 8027571]

Stenn K, Paus R, 2001. Controls of hair follicle cycling. Physiol. Rev 10.1152/physrev.2001.81.1.449.

Straile WE, Chase HB, Arsenault C, 1961. Growth and differentiation of hair follicles between periods of activity and quiescence. J. Exp. Zool 148 (3), 205–221. 10.1002/jez.1401480304. [PubMed: 13917600]

Sun Z, Plikus MV, Komarova NL, 2016. Near equilibrium calculus of stem cells in application to the airway epithelium lineage. PLoS Comput. Biol 12 (7), e1004990. [PubMed: 27427948]

Takahashi H, Ikeda T, 1996. Transcripts for two members of the transforming growth factor-β superfamily BMP-3 and BMP-7 are expressed in developing rat embryos. Dev. Dyn 207 (4), 439–449. 10.1002/(SICI)1097-0177(199612)207:4<439::AID-AJA8>3.0.CO;2-I. [PubMed: 8950518]

Van Mater D, Kolligs FT, Dlugosz AA, Fearon ER, 2003. Transient activation of β-catenin signaling in cutaneous keratinocytes is sufficient to trigger the active growth phase of the hair cycle in mice. Genes Dev. 17 (10), 1219–1224. [PubMed: 12756226]

Van Scott E, Ekel T, Auerbach R, 1963. Determinants of rate and kinetics of cell division in scalp hair. J. Invest. Dermatol 41 (5), 269–273. [PubMed: 14075450]

Vidal VP, Chaboissier M-C, Lützkendorf S, Cotsarelis G, Mill P, Hui C-C, Ortonne N, Ortonne J-P, Schedl A, 2005. Sox9 is essential for outer root sheath differentiation and the formation of the hair stem cell compartment. Curr. Biol 15 (15), 1340–1351. [PubMed: 16085486]

Wang LC, Liu Z-Y, Shapiro R, Yang J, Sizing I, Rayhorn P, Garber EA, Benjamin CD, Williams KP, Taylor FR, et al. , 2000. Conditional disruption of hedgehog signaling pathway defines its critical role in hair development and regeneration. J. Invest. Dermatol 114 (5), 901–908. 10.1046/j.1523-1747.2000.00951.x. [PubMed: 10771469]

Wang Q, Oh JW, Lee H-L, Dhar A, Peng T, Ramos R, Guerrero-Juarez CF, Wang X, Zhao R, Cao X, et al. , 2017. A multi-scale model for hair follicles reveals heterogeneous domains driving rapid spatiotemporal hair growth patterning. Elife 6.

Warne DJ, Baker RE, Simpson MJ, 2019. Simulation and inference algorithms for stochastic biochemical reaction networks: from basic concepts to state-of-the-art. J. R. Soc. Interface 16 (151), 20180943. [PubMed: 30958205]

Weedon D, Strutton G, 1981. Apoptosis as the mechanism of the involution of hair follicles in catagen transformation. Acta Dermato-Venereol. 61 (4), 335–339.

Yang C-C, Cotsarelis G, 2010. Review of hair follicle dermal cells. J. Dermatol. Sci 57 (1), 2–11. 10.1016/j.jdermsci.2009.11.005. [PubMed: 20022473]

Yue Z, Lei M, Paus R, Chuong C-M, 2021. The global regulatory logic of organ regeneration: circuitry lessons from skin and its appendages. Biol. Rev 96 (6), 2573–2583. [PubMed: 34145718]

Zamil MS, Harland DP, Fisher BK, Davis MG, Schwartz JR, Geitmann A, 2021. Biomechanics of hair fibre growth: A multi-scale modeling approach. J. Mech. Phys. Solids 148, 104290.

Zhang H, Nan W, Wang S, Zhang T, Si H, Yang F, Li G, 2016. Epidermal growth factor promotes proliferation and migration of follicular outer root sheath cells via Wnt/β-catenin signaling. Cell. Physiol. Biochem 39 (1), 360–370. [PubMed: 27352380]

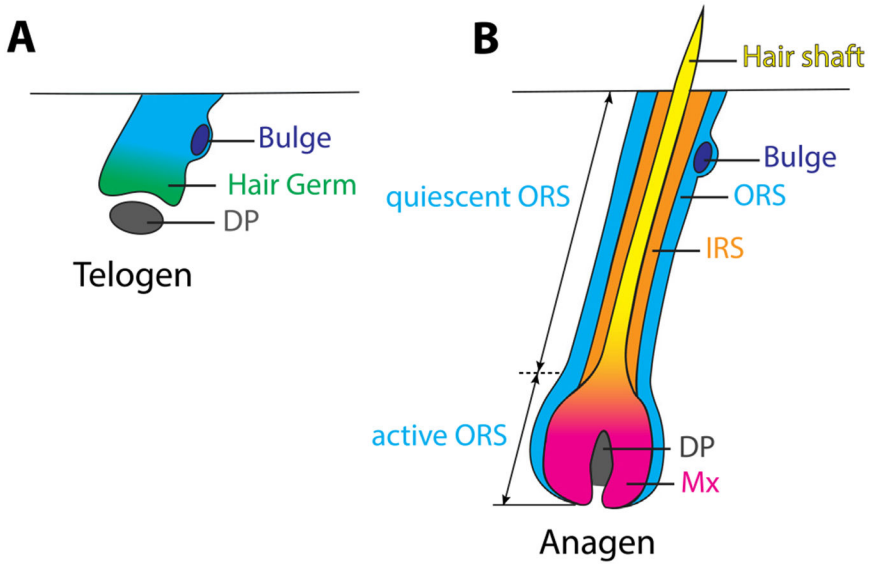

Fig. 1.
Illustration of a hair follicle (HF) in telogen (A) and anagen (B).

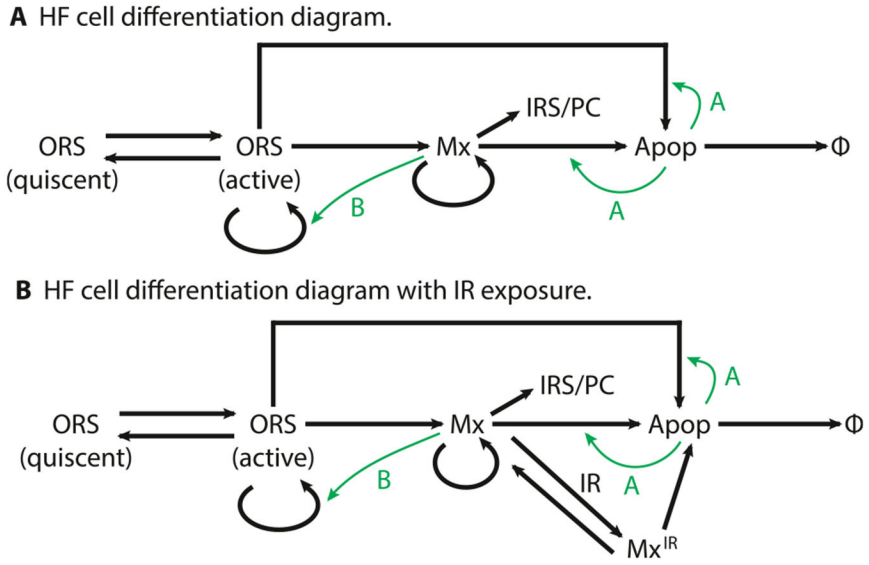

Fig. 2.

A HF cell differentiation diagram during anagen, with green arrows indicating the feedback controls. **B** HF cell differentiation diagram with IR exposure: upon IR exposure, all current Mx cells turn into Mx^{IR} cells, after that, Mx^{IR} cells either return to normal Mx cells or start apoptosis.

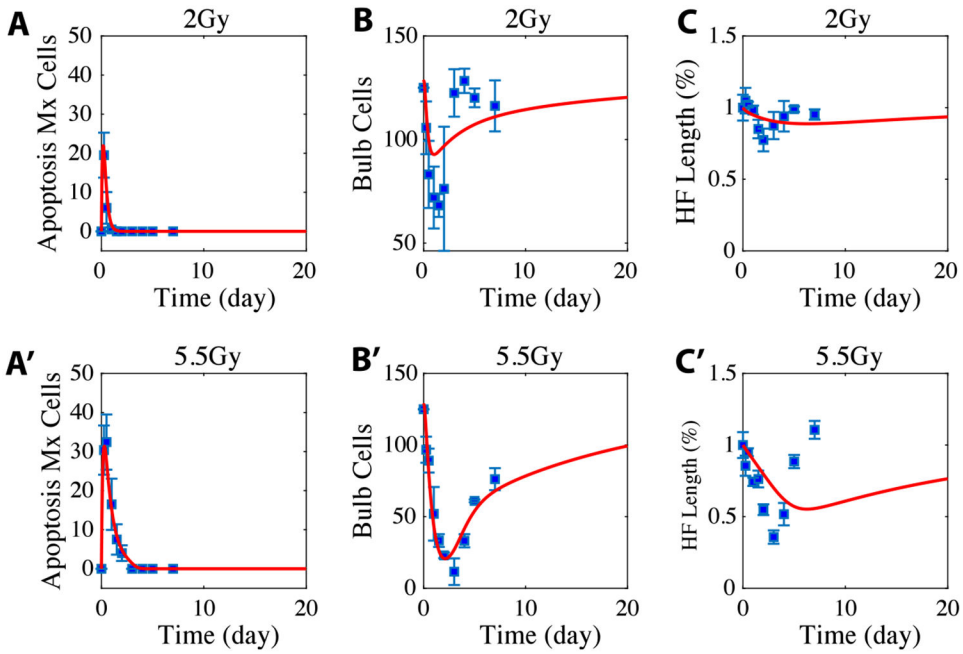

Fig. 3.

Parameter calibration of the IR induced HF regeneration model. Red lines show simulation results, blue boxes show experimental data. **ABC** show simulations/experimental observations with 2 Gy IR, and **A′B′C′** show simulations/experimental observations with 5.5 Gy IR. Parameters are calibrated to apoptotic Mx cells (**AA′**), bulb cells (**BB′**) and the percentage of HF length (**CC′**)—modeled as the ratio of current ORS cell number to that in controlled mice.

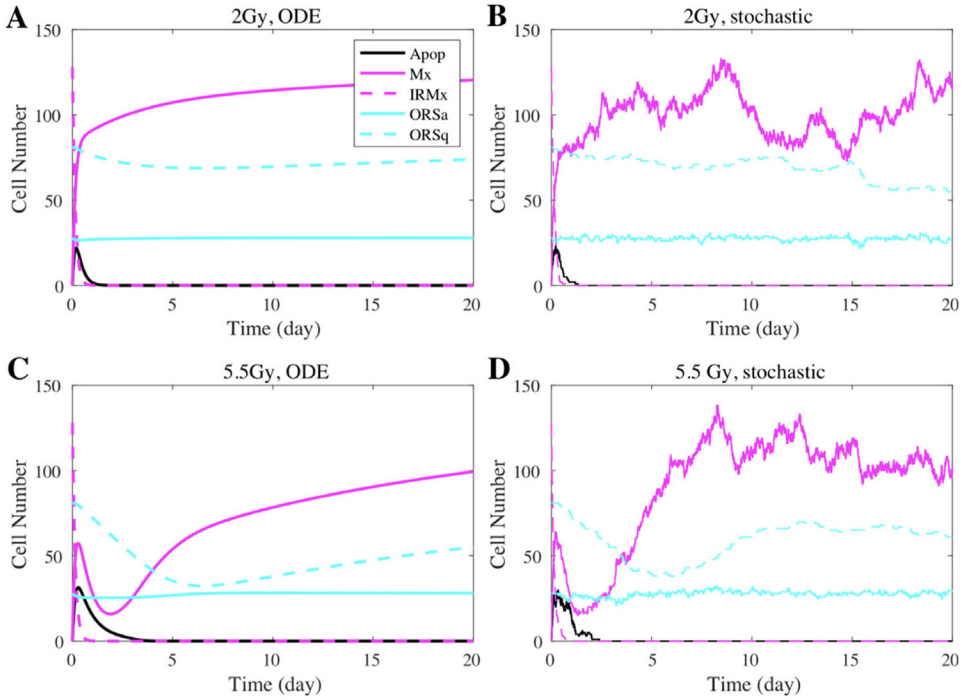

Fig. 4.

Simulations of IR induced HF regenerative dynamics. **AB** 2 Gy IR, **CD** 5.5 Gy IR. **AC** show the results from the ODE simulations, **BD** show sample paths from the stochastic simulations.

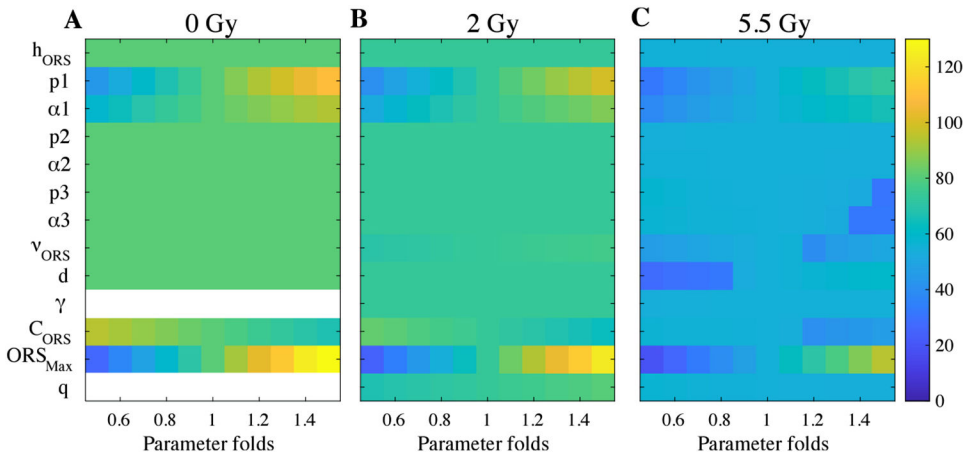

Fig. 5.

Sensitivity of the parameters. At each time, only one parameter value changes, ranged from 0.5- to 1.5-fold of the calibrated value. Heatmap shows the number of quiescent ORS cells (ORS_q) at day 20, as a measure of the HF regeneration ability. Simulations are taken from **A** 0 Gy IR, no radiation, **B** 2 Gy IR and **C** 5.5 Gy IR models. In 0 Gy simulations, we use the calibrated values of α_2, p_2, α_3, p_3 from the 2 Gy IR data.

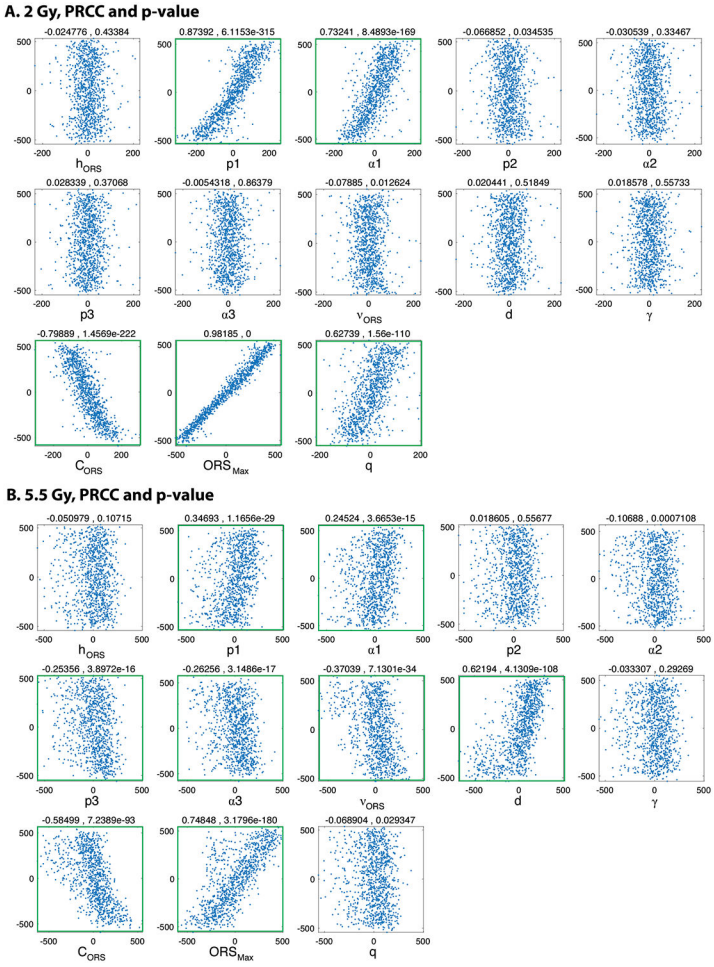

Fig. 6.

PRCC performed on the (**A**) 2 Gy and (**B**) 5.5 Gy IR models. Parameter values are sampled using LHS, with each parameter uniformly distributed between 0.5 to 1.5 folds of the calibrated value. The first/second index on top of each panel shows the PRCC/*p*-value of that parameter. Parameters showing large PRCC and small *p*-value are highlighted by the green boxes.

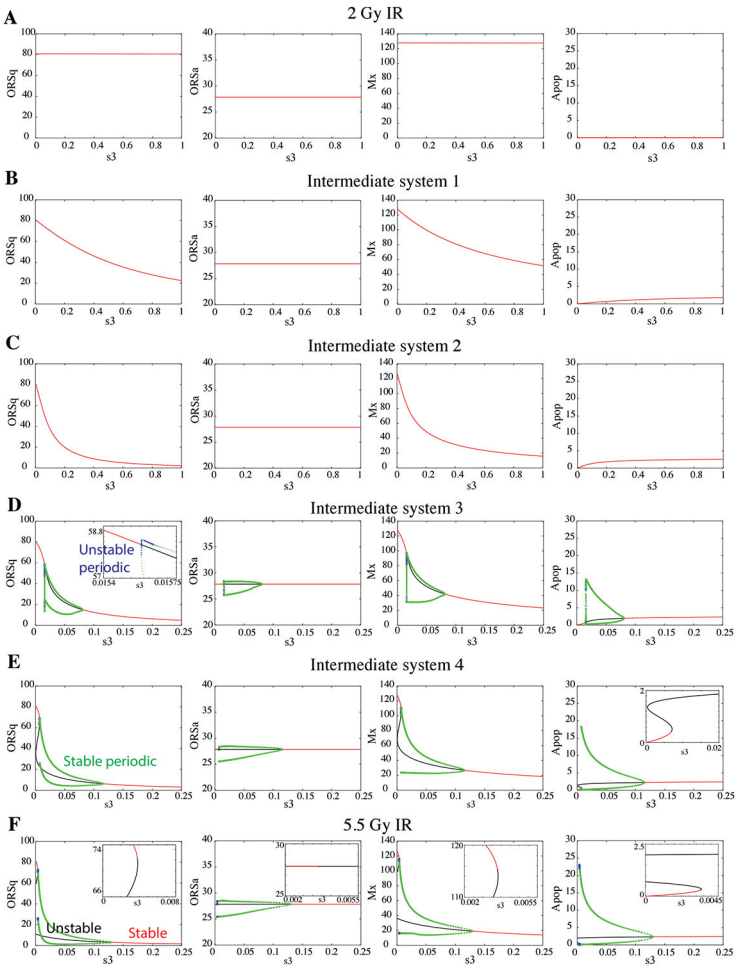

Fig. 7.

Bifurcation diagrams of the HF regeneration dynamics with respect to the Mx cells' spontaneous apoptosis rate s_3. **A**, 2 Gy IR system. **BCDE**, intermediate systems 1–4, **F** 5.5 Gy IR system. Parameter values of p_2, p_3, α_2, α_3 of the systems are provided in Table E.3. Red solid line—stable state, black solid line—unstable state, green dots—stable periodic solution, blue circles—unstable periodic solution. A close up view in **D** shows a small region of unstable periodic solution. Close up views of the stable (red) and unstable (black) solutions near the anagen HF homeostatic state are shown in **F**, with the dots indicating periodic solutions removed.

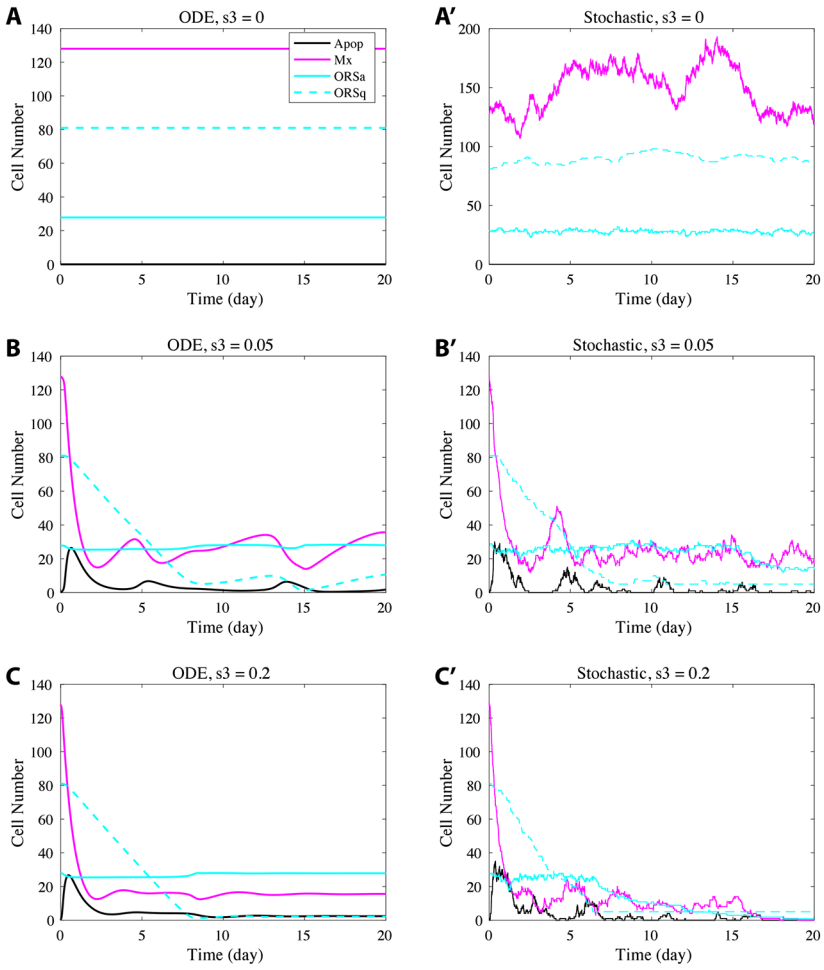

Fig. 8.

Dynamic simulations of the HF cell population system with different Mx spontaneous apoptosis rate values (s_3). **AA′**, $s_3 = 0$, no spontaneous apoptosis in Mx cells, HF stays in the stable homeostatic state. **BB′**, $s_3 = 0.05$, HF degenerates, followed by small amplitude periodic dynamics. **CC′**, $s_3 = 0.2$, HF fully degenerates. **ABC**, ODE simulations. **A′B′C′**, stochastic simulations.

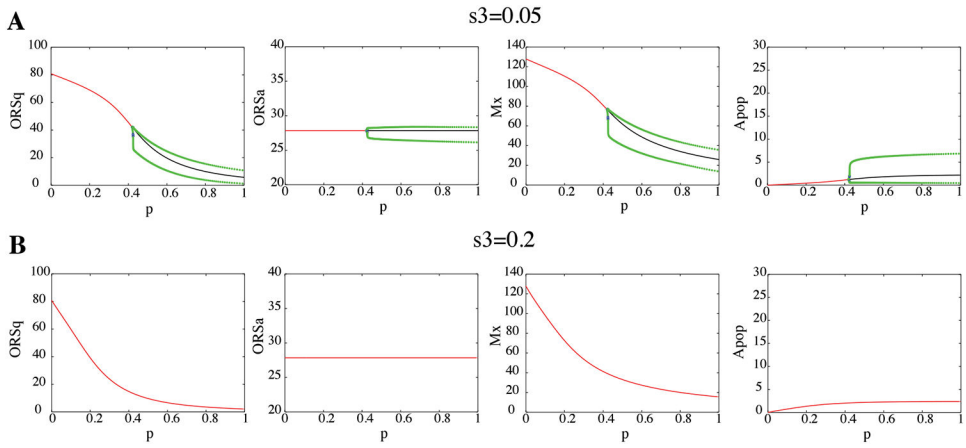

Fig. 9.

Bifurcation diagrams of the HF regeneration dynamics with respect to the apoptosis feedback strength $p = p_2 = p_3$. α_2, α_3 values are taken from the 5.5 Gy IR system. **A**, $s_3 = 0.05$. **B**, $s_3 = 0.2$.

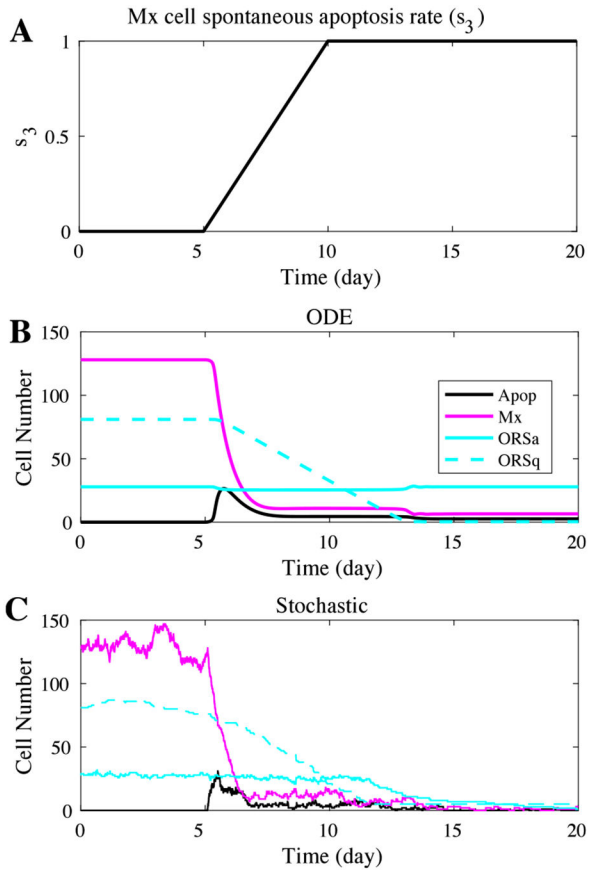

Fig. 10.

Simulation of the anagen-to-catagen transition dynamics. **A** At day 5, s_3 increases linearly, causing the degeneration of the HF epithelium. **B** ODE simulation results, **C** a sample path from the stochastic simulation. p_2, α_2, p_3, α_3 values are taken from the 5.5 Gy IR system.